



ICAM

Institute for Computational
and Applied Mechanics

INTERIM
IN 34-2R
ICIT.
30943
P-54

RADIATIVE INTERACTIONS IN CHEMICALLY REACTING COMPRESSIBLE NOZZLE FLOWS USING MONTE CARLO SIMULATIONS

By

J. Liu and S. N. Tiwari (Principal Investigator)

(NASA-CR-197133) RADIATIVE
INTERACTIONS IN CHEMICALLY REACTING
COMPRESSIBLE NOZZLE FLOWS USING
MONTE CARLO SIMULATIONS Progress
Report, Jan. - Jun. 1994 (Old
Dominion Univ.) 54 p

N95-15966

Unclas

G3/34 0030943

NASA Grant NAG-1-363
NASA Langley Research Center
Hampton, Virginia 23681-0001

ODU/ICAM Report 94-102
September 1994

Old Dominion University
Norfolk, Virginia 23529-0247

FOREWORD

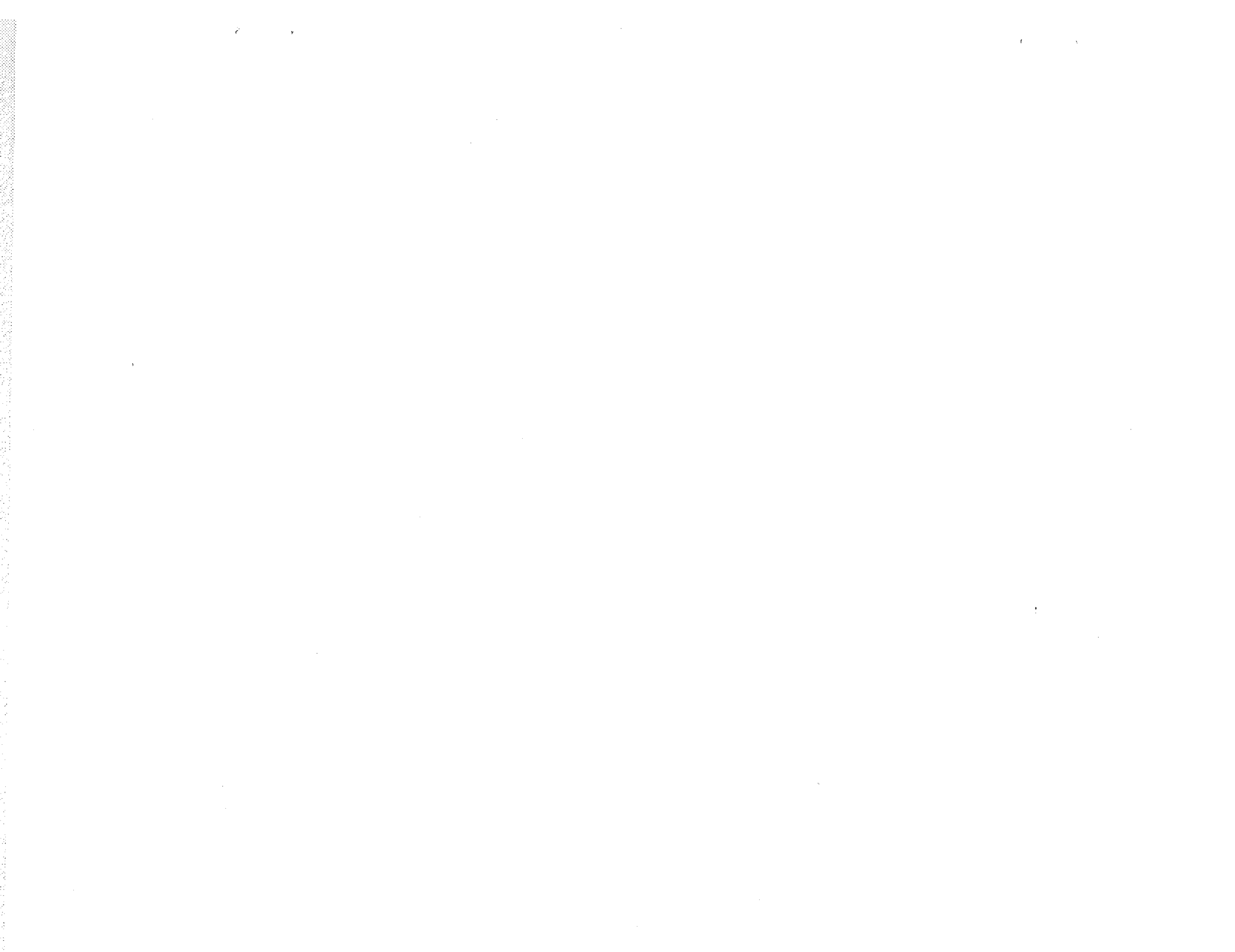
This research work was conducted in cooperation with the Theoretical Flow Physics Branch of the Fluid Mechanics Division of NASA Langley Research Center and the Institute for Computational and Applied Mechanics (ICAM) of Old Dominion University. The study was a part of the research project on "Analysis and Computation of Internal Flow Field in a Scramjet Engine." Specific work on this study was conducted during the period January through June 1994. During this period, attention was directed to "Radiative Interactions in Chemically Reacting Compressible Nozzle Flows Using Monte Carlo Simulations." Important results of this study were presented at the 6th AIAA/ASME Joint Thermophysics and Heat Transfer Conference, Colorado Springs, Colorado, June 20-23, 1994; AIAA Paper No. 94-2092, June 1994 (see Appendix A).

The authors are indebted to Drs. Ajay Kumar and J. P. Drummond of the Theoretical Flow Physics Branch for their cooperation and technical assistance.

This work was supported, in part, by the Old Dominion University's ICAM Program through NASA Grant NAG-1-363. The grant was monitored by Mr. Edwin J. Prior, University Affairs Officer, NASA Langley Research Center, Hampton, Virginia 23681-0001.

TABLE OF CONTENTS

	<u>Page</u>
FOREWORD	iii
ABSTRACT	1
NOMENCLATURE	1
INTRODUCTION	3
GENERAL FORMULATION	6
Governing Equations	7
Thermodynamic and Chemistry Models	8
RADIATION TRANSFER MODEL	10
METHOD OF SOLUTION	13
RESULTS AND DISCUSSION	14
CONCLUSIONS	20
ACKNOWLEDGEMENT	20
REFERENCES	20
APPENDIX A: AIAA-94-2092	36



RADIATIVE INTERACTIONS IN CHEMICALLY REACTING COMPRESSIBLE NOZZLE FLOWS USING MONTE CARLO SIMULATIONS

J. Liu¹ and S. N. Tiwari²

Department of Mechanical Engineering
Old Dominion University, Norfolk, VA 23529-0247

ABSTRACT

The two-dimensional spatially elliptic Navier-Stokes equations have been used to investigate the radiative interactions in chemically reacting compressible flows of premixed hydrogen and air in an expanding nozzle. The radiative heat transfer term in the energy equation is simulated using the Monte Carlo method (MCM). The nongray model employed is based on the statistical narrow band model with an exponential-tailed inverse intensity distribution. The spectral correlation has been considered in the Monte Carlo formulations. Results obtained demonstrate that the effect of radiation on the flowfield is minimal but its effect on the wall heat transfer is significant. Extensive parametric studies are conducted to investigate the effects of equivalence ratio, wall temperature, inlet flow temperature, and the nozzle size on the radiative and conductive wall fluxes.

NOMENCLATURE

Latin Symbols

A	reaction rate constant; also area, m ²
C	concentration, kg.mole/m ³
C _p	specific heat, J/(kg.K)
D	diffusion coefficient, m ² /s
E	total internal energy, J/kg; also activation energy, J/kg
f	mass fraction
g	Gibbs energy, J/(kg.K)

¹ Graduate Research Assistant. Student Member ASME.

² Eminent Professor. Fellow ASME.

h	static enthalpy, J/kg
h^R	base enthalpy, J/kg
I_ω	spectral radiative intensity, kW/(m ² .sr.cm ⁻¹)
k	thermal conductivity, J/(m.s.k); also line intensity to spacing ratio, cm ⁻¹ . atm ⁻¹
k_b	backward rate constant
k_{eq}	equilibrium constant
k_f	forward rate constant
L	nozzle length, m
m_ω	total number of narrow bands
M	molecular weight
N	temperature coefficient in reaction rate expression
N_s	number of species
N_r	number of reactions
p	gas pressure, atm
q_{cw}	conductive wall flux, kW/m ²
$-\nabla \cdot q_r$	radiative source term, kW/m ³
q_{rw}	net radiative wall flux, kW/m ²
Q	radiative energy per unit volume, kW/m ³
R	gas constant, J/(kg.K); also random number
R_u	universal gas constant, J/(kg.K)
s, s', s''	position variables, m
t	time, s
T	absolute temperature, K
u	velocity in x direction, m/s
\tilde{u}	diffusion velocity in x direction, m/s
v	velocity in y direction, m/s
\tilde{v}	diffusion velocity in y direction, m/s
\tilde{V}	diffusion velocity vector, m/s
\dot{w}	production rate of species, kg/(m ³ .s)
x	x-coordinate, m
X	mole fraction

y	y-coordinate, m
y_b	half height of cross sectional area of nozzle, m
Greek symbols	
β	line width to spacing ratio
γ	stoichiometric coefficient; also half-width of an absorption line, cm^{-1}
δ	equivalent line spacing, cm^{-1}
θ	polar angle
μ	dynamic viscosity, $\text{kg}/(\text{m}\cdot\text{s})$
ξ, η	computational coordinates
ρ	density, kg/m^3
σ	normal stress, N/m^2
τ	shear stress, N/m^2
τ_ω	spectral transmittance
ϕ	equivalence ratio
ψ	azimuthal angle
ω	wavenumber, cm^{-1}
Ω	solid angle

INTRODUCTION

There has been extensive research underway to develop hydrogen-fueled supersonic combustion ramjet (scramjet) propulsion systems for National Aero-Space Plane (NASP). A critical element in the design of scramjets is the detailed understanding of the complex flowfield present in different regions of the system over a range of operating conditions. Numerical modeling of the flow in various sections has shown to be a valuable tool for gaining insight into the nature of these flows.

In a hypersonic propulsion system, combustion takes place at supersonic speeds to reduce the deceleration energy loss. The products of hydrogen-air combustion are gases such as water vapor and hydroxyl radical. These species are highly radiatively absorbing and emitting. Thus, numerical simulation must be able to correctly handle the radiation phenomena associated with supersonic flows.

The study of radiative transmission in nonisothermal and inhomogeneous nongray gaseous systems requires a detailed knowledge of the absorption, emission and scattering characteristics of the specific species under investigation. In absorbing and emitting media, an accurate nongray model is of vital importance in the correct formulation of the radiative flux equations. The line-by-line models are theoretically the most precise models to treat radiative heat transfer. But solutions of the line-by-line formulation require considerably large computational resources. Currently, it is not practical to apply the line-by-line models in most engineering problems. The wide band models are the simplest nongray models and are extensively used in radiative heat transfer analyses [1, 2]. By far the most popular wide band model is the exponential wide band model developed by Edwards [3]. The exponential wide band model accounts for discrete absorption bands and spectral correlations resulting from the high resolution structure. However, the spectral discretization used in this model is too wide and it does not take into account the low resolution correlations between intensities and transmissivities [4, 5]. Also, the case of partially reflecting walls cannot be correctly modelled with this approach [3]. Recently, the narrow band models have begun to receive a lot of attention due to the strong requirement for accurate simulation of radiation. Some narrow band models can compare favorably to the line-by-line calculations [4, 6], and they are much simpler than the line-by-line models. In addition, the narrow band models do not have disadvantages usually encountered with the wide band models.

Most of the existing analyses in radiative heat transfer start with the radiative transfer equation. Use of a narrow band model in this equation results in two types of spectral correlations [7]. One is the spectral correlation between the intensity and the transmittance within the medium. Another is the spectral correlation between the reflected component of the wall radiosity and the transmittance. In order to investigate the first type of spectral correlation, all the intermediate transmittances in each finite volume element of medium along the path the radiative energy travels must be calculated and stored to make a correlated calculation. In order to investigate the second type of spectral correlation, a series expansion of the wall radiosity is required [8, 9]. Essentially, this series expansion is utilized along with a technique for closure of the series.

Consideration of the history of a finite number of reflections and approximating the remaining reflections by a closure method in the radiative transfer equation complicates the mathematical formulation and increases the computer time considerably. As the geometry considered becomes complicated, exact simulation of radiative heat transfer by most existing methods becomes very difficult for the cases with reflecting walls.

The MCM is not directly based on the radiative transfer equation to simulate radiative heat transfer. This results in the MCM having features different from the other methods for narrow band analysis. When the radiative energy is transmitted in the medium, the spectral correlation only occurs between the transmittances of two different segments of the same path in the statistical relationship for determining the absorption location of a energy bundle [10]. For the case with reflecting walls, Monte Carlo treatment with a narrow band model is similar to that with a gray model, and the second type of spectral correlation occurring in other methods does not exist. If the effect of scattering is included, a new type of spectral correlation occurs in the scattering term of the radiative transfer equation. Treatment of this spectral correlation will be far more complicated than the second type of spectral correlation mentioned earlier. In such cases, it has been indicated that only MCM can account for scattering in a correlated manner [11].

The objective of present study is to apply the Monte Carlo formulations with a narrow band model to investigate the effects of radiation on multi-dimensional chemically reacting supersonic flows. Only a limited number of studies are available to investigate the interaction of radiation heat transfer in chemically reacting viscous and supersonic flows of molecular species. Mani and Tiwari [12] are the first to take into account the effects of radiation in chemically reacting supersonic flows. This work has been extended to include relatively more advanced chemistry models by Tiwari et al. [13]. In both of these studies, a tangent slab approximation was employed with a gray gas model. This approximation treats the gas layer as a one-dimensional slab in evaluation of the radiative flux. Obviously, it is impossible to obtain reliable quantitative predictions of radiation from this treatment. In this study, one of the most accurate nongray models available is employed and multi-dimensional radiative heat transfer is simulated exactly

using the MCM; the results of radiative flux are then incorporated in the Navier-Stokes equations. This procedure provides a more accurate prediction of the radiative effects than the previous studies.

GENERAL FORMULATION

Governing Equations

The physical model considered is a supersonic flow of premixed hydrogen and air in an expanding nozzle (Fig.1). The nozzle wall is defined, as noted, by a shifted sinusoidal curve. The inlet temperatures of hydrogen and air are considerably high so that the chemical reaction takes place in the entire flowfield. The products of hydrogen-air combustion include water vapor and hydroxyl radical. These species are highly absorbing and emitting. To simulate the flowfield accurately, all important phenomena such as chemistry, radiation and turbulence should be taken into account. In this study, the two-dimensional nozzle flow considered is described by the Navier Stokes and species continuity equations which take the form in the physical coordinates as

$$\frac{\partial U}{\partial t} + \frac{\partial F}{\partial x} + \frac{\partial G}{\partial y} = H \quad (1)$$

where vectors U, F, G and H are represented by

$$U = \begin{bmatrix} \rho \\ \rho u \\ \rho v \\ \rho E \\ \rho f_j \end{bmatrix} \quad (2)$$

$$F = \begin{bmatrix} \rho u \\ \rho u^2 - \sigma_x \\ \rho uv - \tau_{yx} \\ (\rho E - \sigma_x)u - \tau_{xy}v + q_x \\ \rho f_i(u + \tilde{u}_i) \end{bmatrix} \quad (3)$$

$$G = \begin{bmatrix} \rho v \\ \rho uv - \tau_{xy} \\ \rho v^2 - \sigma_y \\ (\rho E - \sigma_y)v - \tau_{yx}u + q_y \\ \rho f_i(v + \tilde{v}_i) \end{bmatrix} \quad (4)$$

$$H = \begin{bmatrix} 0 \\ 0 \\ 0 \\ -\nabla \cdot q_r \\ \dot{w}_i \end{bmatrix} \quad (5)$$

The other terms appearing in vectors F, G, and H are defined as

$$\sigma_x = -p + \lambda \left(\frac{\partial u}{\partial x} + \frac{\partial v}{\partial y} \right) + 2\mu \frac{\partial u}{\partial x} \quad (6)$$

$$\sigma_y = -p + \lambda \left(\frac{\partial u}{\partial x} + \frac{\partial v}{\partial y} \right) + 2\mu \frac{\partial v}{\partial y} \quad (7)$$

$$\tau_{xy} = \tau_{yx} = \mu \left(\frac{\partial u}{\partial x} + \frac{\partial v}{\partial y} \right) \quad (8)$$

$$q_x = -k \frac{\partial T}{\partial x} + \rho \sum_{i=1}^{N_s} h_i f_i \tilde{u}_i \quad (9)$$

$$q_y = -k \frac{\partial T}{\partial y} + \rho \sum_{i=1}^{N_s} h_i f_i \tilde{v}_i \quad (10)$$

$$E = -\frac{p}{\rho} + \frac{u^2 + v^2}{2} + \sum_{i=1}^{N_s} h_i f_i \quad (11)$$

$$h_i = h_i^R + \int_{T_R}^T C_{p,i} dT \quad (12)$$

$$p = \rho R_u T \sum_{i=1}^{N_s} \frac{f_i}{M_i} \quad (13)$$

where $\lambda = -\frac{2}{3}\mu$, $\mu = \mu_l + \mu_t$ and $k = k_l + k_t$. In this study the molecular viscosity μ_l and molecular thermal conductivity k_l are evaluated from the Sutherland's law [14]; the turbulent viscosity μ_t is evaluated from the Baldwin-Lomax model and the turbulent thermal conductivity k_t is calculated from the turbulent Prandtl number.

In Eq. (1), only (N_s-1) species equations need to be considered since the mass fraction of the species is prescribed by satisfying the constraint equation

$$\sum_{i=1}^{N_s} f_i = 1 \quad (14)$$

The diffusion velocity of the i th species is obtained by solving the Stefan-Maxwell equation [15], neglecting the body force and thermal diffusion effects, as

$$\nabla X_i = \sum_{j=1}^{N_s} \left(\frac{X_i X_j}{D_{ij}} \right) (\tilde{V}_j - \tilde{V}_i) + (f_i - X_i) \left(\frac{\nabla p}{p} \right) \quad (15)$$

where $D_{ij} = D_{ij}^l + D_{ij}^t$. The molecular diffusion coefficient D_{ij}^l is obtained from the kinetic theory [15] and the turbulent diffusion coefficient D_{ij}^t is evaluated from the turbulent Schmidt number. Equation (15) has to be applied only to (N_s-1) species. The diffusion velocity for the remaining species is prescribed by satisfying the constraint equation $\sum_{i=1}^{N_s} f_i \tilde{V}_i = 0$, which ensures the consistency.

In the energy equation, it is noted that the radiative source term $-\nabla \cdot q_r$ has been moved to the right hand side and its treatment will be different from other terms. The simulation of this source term will be explained in detail later.

Thermodynamic and Chemistry Models

The specific heat of individual species C_{p_i} is defined by a fourth-order polynomial in temperature,

$$\frac{C_{p_i}}{R} = A_i + B_i T + C_i T^2 + D_i T^3 + E_i T^4 \quad (16)$$

The values of the coefficients appearing in Eq. (16) are found in [16]. Knowing the specific heat of each species, the enthalpy of each species can be found from Eq. (12) and the total internal energy is computed from Eq. (11).

Chemical reaction rate expressions are usually determined by summing the contributions from each relevant reaction path to obtain the total rate of change of each species. Each path is governed by a law of mass action expression in which the rate constants can be determined from a temperature dependent Arrhenius expression. In vector H , the term $\dot{w}_i = M_i C_i$ represents the net rate of production of species i in all chemical reactions and is modelled as follows:

$$\sum_{i=1}^{N_s} \gamma'_{ij} C_j \stackrel{k_{f_j}}{=} \sum_{i=1}^{N_s} \gamma''_{ij} C_j; \quad j = 1, \dots, N_r \quad (17)$$

$$\dot{w}_i = M_i C_i = M_i \sum_{j=1}^{N_r} (\gamma''_{ij} - \gamma'_{ij}) \left[k_{f_j} \prod_{m=1}^{N_s} C_m^{\gamma'_{jm}} - k_{b_j} \prod_{m=1}^{N_s} C_m^{\gamma''_{jm}} \right] \quad (18)$$

Equation (17) represents an N_r step chemical reaction and Eq. (18) is the production rate for the i th species. The reaction constants k_{f_j} and k_{b_j} are calculated from the following equations:

$$k_{f_j} = A_j T^{N_j} \exp\left(-\frac{E_j}{R_u T}\right); \quad j = 1, \dots, N_r \quad (19)$$

$$k_{b_j} = k_{f_j} / k_{eq_j}; \quad j = 1, \dots, N_r \quad (20)$$

The equilibrium constant appearing in Eq. (20) is given by

$$k_{eq_j} = \left(\frac{1}{R_u T}\right)^{\Delta n_j} \exp\left(\frac{-\Delta G_{R_j}}{R_u T}\right); \quad j = 1, \dots, N_r \quad (21)$$

where

$$\Delta n_j = \sum_{i=1}^{N_s} \gamma''_{ij} - \sum_{i=1}^{N_s} \gamma'_{ij}; \quad j = 1, \dots, N_r \quad (22)$$

$$\Delta G_{R_j} = \sum_{i=1}^{N_s} \gamma''_{ij} g_i - \sum_{i=1}^{N_s} \gamma'_{ij} g_i; \quad j = 1, \dots, N_r \quad (23)$$

$$\begin{aligned} \frac{g_i}{R_i} = & A_i(T - \ln T) - \frac{B_i}{2}T^2 - \frac{C_i}{6}T^3 - \frac{D_i}{12}T^4 \\ & - \frac{E_i}{20}T^5 + F_i - G_iT; \quad i = 1, \dots, N_r \end{aligned} \quad (24)$$

The forward rate for each reaction is determined from Eq. (19). The hydrogen-air combustion mechanism used in this work is from [17], but only seven species and seven reactions are selected for this study. The constants A_j , N_j and E_j for these reactions are listed in Table 1. The coefficients for the Gibb's free energy in Eq. (24) are available in [16].

RADIATION TRANSFER MODEL

The effects of radiation on the heat transfer to the nozzle flow and wall arise through the term $-\nabla \cdot q_r$ in the energy equation and the net radiative wall flux q_{rw} . The expressions for both $-\nabla \cdot q_r$ and q_{rw} are very complicated integro-differential equations and they are usually treated separately from Eq. (1). Before applying MCM to evaluate $-\nabla \cdot q_r$ and q_{rw} , temperature, concentration of species, and pressure in the media should be assumed. Next, the participating media and the surrounding walls are divided into many rectangular volume elements and surface elements (Fig. 2). Note that the inlet and outlet surfaces of the nozzle flow are treated as pseudoblack walls with the same temperature as the local gas. Use of a rectangular volume element rather than other geometrical element can simplify the Monte Carlo simulation. However, it also introduces the problem that the nozzle walls do not fall on the control volume faces of the computational domain. In this study these curved boundaries are approximated with ladder-like lines [18] as shown in Fig. 2. This practice enables the modeling of complex geometries in Cartesian coordinates system. Errors in the approximations of these boundaries can be reduced by using finer computational elements.

For an arbitrarily chosen volume element ABCD with a volume δV and an arbitrarily chosen surface element EF with an area δA (Fig. 2), the relations for $-\nabla \cdot q_r$ and q_{rw} are expressed as

$$-\nabla \cdot q_r = \frac{Q_{V-\delta V} + Q_{A-\delta V} - Q_{\delta V}}{\delta V} \quad (25)$$

$$q_{rw} = \frac{Q_{V-\delta A} + Q_{A-\delta A} - Q_{\delta A}}{\delta A} \quad (26)$$

Here, $Q_{V-\delta V}$ and $Q_{V-\delta A}$ are the total radiant energy from the entire gas that are absorbed by the volume element δV and surface element δA , respectively; $Q_{A-\delta V}$ and $Q_{A-\delta A}$ are the total radiant energy from the bounding walls that are absorbed by δV and δA , respectively; $Q_{\delta V}$ and $Q_{\delta A}$ are the radiant energy emitted by δV and δA , respectively.

Evaluation of the terms $Q_{V-\delta V}$, $Q_{A-\delta V}$, $Q_{\delta V}$ and $Q_{V-\delta A}$ in Eqs. (25) and (26) requires a detailed knowledge of the absorption, emission and scattering characteristics of the specific gas. Several models are available in the literature to represent the absorption emission characteristics of molecular species. An accurate nongray model employed in this study is the statistical narrow band model with an exponential-tailed inverse intensity distribution and the transmittance of a homogeneous and isothermal column of length l due to gas species j , averaged over $[\omega - (\Delta\omega/2), \omega + (\Delta\omega/2)]$, is then given by [19]

$$\bar{\tau}_{\omega}^j = \exp \left[-\frac{\bar{\beta}}{\pi} \left(\sqrt{\left(1 + \frac{2\pi X_j p l \bar{k}}{\bar{\beta}} \right)} - 1 \right) \right] \quad (27)$$

where X_j represents the mole fraction of the absorbing species j ; \bar{k} and $\bar{\beta} = 2\pi\bar{\gamma}/\bar{\delta}$ are the band model parameters which account for the spectral structure of the gas. The overbar symbol indicates that the quantity is averaged over a finite wavenumber interval $\Delta\omega$. Parameters \bar{k} and $1/\bar{\delta}$ generated from a line-by-line calculation have been published for H₂O and CO₂ [6, 20, 21]. The mean half-width $\bar{\gamma}$ is obtained using the parameters suggested by Soufiani et al. [6]. The narrow band width considered is usually 25 cm⁻¹. Nonisothermal and inhomogeneous media are treated by using the Curtis-Godson approximation [22].

To simulate radiative heat transfer using the MCM, the total radiant energy in a volume element or surface element is assumed to be composed of many energy bundles. These energy bundles are similar to photons in their behavior. The histories of these energy bundles are traced from their point of emission to their point of absorption. What happens to each of these bundles depends on the emissive, scattering and absorptive behavior within the medium

which is described by a set of statistical relationships. The detailed discussion of the MCM has been provided by Howell [23]. However, not all the statistical relationships given by Howell are applicable while using narrow band models. An important change is the necessity to spectrally average radiative properties within each narrow band. This results in spectrally correlated formulations. For the volume element ABCD shown in Fig. 2, the total emitted radiant energy and major statistical relationships in conjunction with a narrow band model are given by [24]

$$Q_{\delta V} = \sum_{k=1}^{m_{\omega}} \left\{ \int_0^b \int_0^{\pi} \int_0^{2\pi} \overline{I_{b\omega^k}} [1 - \overline{\tau_{\omega^k}}(s \rightarrow s')] \cos \theta \sin \theta d\psi d\theta dx^* \right\} \Delta\omega^k \quad (28)$$

$$R_{\omega} = \frac{\sum_{k=1}^n \left\{ \int_0^b \int_0^{\pi} \int_0^{2\pi} \overline{I_{b\omega^k}} [1 - \overline{\tau_{\omega^k}}(s \rightarrow s')] \cos \theta \sin \theta d\psi d\theta dx^* \right\} \Delta\omega^k}{Q}, \quad (\omega^{n-1} < \omega \leq \omega^n) \quad (29)$$

$$R_{x^*} = \frac{\sum_{k=1}^{m_{\omega}} \left\{ \int_0^{x^*} \int_0^{\pi} \int_0^{2\pi} \overline{I_{b\omega^k}} [1 - \overline{\tau_{\omega^k}}(s \rightarrow s')] \cos \theta \sin \theta d\psi d\theta dx^* \right\} \Delta\omega^k}{Q} \quad (30)$$

$$R_{\theta} = \frac{\sum_{k=1}^{m_{\omega}} \left\{ \int_0^{\theta} \int_0^b \int_0^{2\pi} \overline{I_{b\omega^k}} [1 - \overline{\tau_{\omega^k}}(s \rightarrow s')] \cos \theta \sin \theta d\psi dx^* d\theta \right\} \Delta\omega^k}{Q} \quad (31)$$

$$R_{\psi} = \frac{\sum_{k=1}^{m_{\omega}} \left\{ \int_0^{\psi} \int_0^b \int_0^{\pi} \overline{I_{b\omega^k}} [1 - \overline{\tau_{\omega^k}}(s \rightarrow s')] \cos \theta \sin \theta d\theta dx^* d\psi \right\} \Delta\omega^k}{Q} \quad (32)$$

$$R_l = \frac{\overline{\tau_{\omega}}(s' \rightarrow s'') - \overline{\tau_{\omega}}(s \rightarrow s'')}{1 - \overline{\tau_{\omega}}(s \rightarrow s')} \quad (33)$$

where $I_{b\omega}$ is the Planck spectral blackbody intensity; x^* is the entering location of the intensity from the side AD which has a length b ; θ and ψ are the polar and azimuthal angles of the intensity over the path $s \rightarrow s'$, respectively; m_{ω} is the total number of narrow bands; R_{ω} , R_{x^*} , R_{θ} , R_{ψ} are random numbers which are uniformly distributed between zero and one. The statistical

relationships for an energy bundle emitted from a surface element are similar to those given by Howell [23] and they are not listed here.

A large number of energy bundles is considered to satisfactorily represent the radiation emitted by a volume or surface element. The total number of energy bundles absorbed by each element multiplied by the energy per bundle gives the interchange of radiation among the volume and /or surface elements. The values of $-\nabla \cdot q_r$ and q_{rw} can then be obtained from Eqs. (25) and (26), respectively. Substituting $-\nabla \cdot q_r$ into the energy equation, Eq. (1) can be solved.

METHOD OF SOLUTION

Equations (1) is written in the the physical domain (x, y) and must be transformed to an appropriate computational domain (ξ, η) for solution. Using an algebraic grid generation technique, a highly clustered grid in the physical domain (near regions where high gradients exist) can be obtained. In the computational domain, Eq. (1) is expressed as

$$\frac{\partial \hat{U}}{\partial t} + \frac{\partial \hat{F}}{\partial \xi} + \frac{\partial \hat{G}}{\partial \eta} = \hat{H} \quad (34)$$

where

$$\begin{aligned} \hat{U} &= UJ, & \hat{F} &= Fy_\eta - Gx_\eta \\ \hat{G} &= Gx_\xi - Fy_\xi, & \hat{H} &= HJ \\ J &= x_\xi y_\eta - y_\xi x_\eta \end{aligned} \quad (35)$$

Here J is the Jacobian of the transformation.

The governing equation system (34) can be stiff due to the kinetic source terms contained in the vector H. To deal with the stiff system, the kinetic source terms are computed implicitly in the temporally discrete form of Eq. (34). Once the temporal discretization is performed, the resulting system is spatially differenced using the explicit, unsplit MacCormack predictor-corrector schemes. This results in a spatially and temporally discrete, simultaneous system of equations at each grid point. Each simultaneous system is solved, subject to initial and boundary conditions. At the supersonic inflow boundary, all flow quantities are specified. At the supersonic

outflow boundary, nonreflective boundary conditions are used. Only the upper half of the flow domain is computed, as the flow is assumed to be symmetric about the centerline of a two-dimensional nozzle. The upper boundary is treated as a solid wall. This implies a non-slip boundary condition. The wall temperature is given and species mass fractions and pressure are extrapolated from interior grid points, by assuming a non-catalytic wall as well as the boundary layer assumption on the pressure gradient. Symmetry boundary conditions are imposed at the lower boundary, that is, at the centerline. Initial conditions are obtained by specifying inlet flow conditions throughout the flowfield. The resulting set of equations is marched in time, until steady state solutions are achieved.

The solution procedure employed in this study is summarized as following: (a) First, the governing equation (1) is solved without consideration of radiation in terms of the modified MacCormack schemes; (b) The steady solutions for temperature, concentration of species and pressure are then used for Monte Carlo simulation. The computed $-\nabla \cdot q_r$ from the MCM is based on a different grid from that used for Eq. (1). Linear interpolation and extrapolation are employed for the transformation of $-\nabla \cdot q_r$ between the two grids; (c) The transformed $-\nabla \cdot q_r$ is substituted into Eq. (1), and Eq. (1) is solved again. If the differences between the new steady solutions and the previous steady solutions are smaller than a designated value, the computation ends. Otherwise, the steps (b) and (c) are repeated until solutions converge. It is noted that there are two levels of numerical procedures employed here which result in two different iterative procedures. One is the numerical procedure for solving the Eq. (1) and solutions iterated with time. The other is the numerical procedure for evaluating the radiative source term using the MCM which results in the iteration of different steady state solutions.

RESULTS AND DISCUSSION

Based on the theoretical and numerical analysis described earlier, a computer code has been developed to simulate two dimensional supersonic chemically reacting and radiating nozzle flows on a Cray X-MP machine. The specific goal in this study is to investigate the effects of radiation on the flowfield and heat flux on the nozzle wall. By referring to [25], several problems have

been considered. They contain four parameters: equivalence ratio of hydrogen and air, inlet flow temperature, wall temperature and nozzle size. Numerical solutions are obtained for a variety of combinations of these parameters. In each problem, flow is introduced to the nozzle at the same velocity of 1230 m/s and the same pressure of 1 atm. The grid size for solving the governing equation is 71×41 . Further refinement of the grid yields little changes in the results. For a given radiative source distribution, the residuals of Eq. (1) are reduced by eight orders of magnitude in 3,000 iterations for a typical case and the steady state solutions are considered to have been obtained. The corresponding CPU time is about six minutes. To check the accuracy of computational scheme, a preliminary calculation has been carried out for chemically reacting nozzle flows without consideration of radiation. The results from this study show very good agreement with available solutions [25, 26].

For the temperature ranges considered, the important radiating species are OH and H₂O. But OH is a much less radiation participating species compared to H₂O. In addition, the concentration of OH is several times less than that of H₂O for the problems considered. So, the contribution of radiation from OH has been neglected in this study. For H₂O, there are five important absorption bands. All these bands have been taken into account and they consist of 295 narrow bands in the spectral range from 150 cm⁻¹ to 7500 cm⁻¹ [20]. In addition, for all the problems considered, the nozzle wall is assumed to be gray and the wall emissivity is taken to be 0.8.

To assure that the statistical results make sense in the Monte Carlo simulation, two requirements must be met. One is the accuracy of statistical results for a given grid. The other is the independence of the results on a grid. In this study, the designated statistical accuracy of the results is defined in such a way that when the relative statistical errors of results are less than $\pm 5\%$, the probability of the results lying within these limits is greater than 95%. Independence of the results on a grid is considered to have been achieved when the volume element number in the x direction is 20 and the volume element number in the y direction varies from 10 to 20 according to different cross-sectional height as shown in Fig. 2. For this grid, the total number of energy bundles had to be 5,000,000 and the required CPU time was about two hours

in order to meet the designated statistical accuracy in results for a typical problem. To test the independence of the Monte Carlo results on the grid, the same problem was investigated with a finer grid in which the volume element number in the x direction was increased to 30 and the volume element number in the y direction was doubled. To obtain the same accurate results, the total number of energy bundles had to increase to 15,000,000 and the corresponding CPU time increased to six hours. Comparing the solutions for the two different grids, it is found that the difference for the net radiative wall flux was never more than 2%, and the difference for the radiative source term was a little higher but less than 10%. In fact, the net radiative wall flux is the quantity we are most interested in, and its accuracy seems more important to us.

The grid considered for Monte Carlo computations in this study is coarser than that for numerical solutions of the energy equation. The intermediate values of the radiative source term within the grid for solutions of Eq. (1) are obtained by interpolation and extrapolation. This should not introduce significant errors as the radiative source term is a slowly varying function compared to the temperature and its derivative [27]. The major CPU time consumed is in the Monte Carlo simulation. Fortunately, Monte Carlo subroutine only need to be called two to three times to obtain the converged steady state solutions. The reason for this will be explained later. It is believed that the computational time for Monte Carlo simulation could be reduced considerably if the code is vectorized and parallelized.

It is a common knowledge that the convective heat transfer is very strong for a supersonic flow. So the effects of radiation may not be very important. To determine these effects quantitatively, a typical problem is selected in which the equivalence ratio of hydrogen and air, wall temperature, inlet flow temperature and the nozzle length are taken to be $\phi=1.0$, $T_w=1900$ K, $T_i=1900$ K and $L=2.0$ m, respectively. Figures 3(a)-3(c) show the temperature, pressure and H_2O mass fraction distributions which are essential information to analyze the effect of radiative heat transfer. Similar trends in results for temperature, pressure and H_2O mass fraction are also observed for other cases considered. As the premixed mixture of hydrogen and air enters the nozzle, an exothermic chemical reaction takes place immediately, and the temperature and

pressure increase abruptly and reach their peaks in a region closer to the inlet location (Figs. 3(a) and 3(b)). During this rapid change in temperature and pressure, the mass fraction of H₂O also experiences a big jump from zero to a value which varies little in the rest of the flow regime (Fig. 3(c)). As the flow continues to move downstream, supersonic expansion plays a major role, and the temperature and pressure are decreased. At the same time, the chemical reaction proceeds but it becomes very weak. This is why there is a little change in H₂O mass fraction in the downstream region.

Figure 4 shows the radiative source distributions at three different locations for the case considered in Figs. 3(a)-3(b). At the location $x/L=0.1$, temperature and pressure are very high and there is more radiant energy emitted than absorbed. Consequently, the radiative source distribution is higher than at locations $x/L=0.5$ and 0.9 . The trend in results for $-\nabla \cdot q_r$ at the location $x/L=0.1$ is seen to be different from the results of other locations due to a decrease in temperature as the distance from the center line increases. The convective heat transfer distributions for the same locations as in Fig. 4 have been also calculated but they are not plotted in Fig. (4). This is because of large differences between the convective and radiative results; and also due to opposite signs for convective results at different locations. In most regions, the absolute value of the convective heat transfer is two or three orders of magnitude larger than the radiative source term. This situation does not change as long as the speed of the flow is very high. So, the effects of radiation on the flowfield are very weak for supersonic flows. This confirms our expectation and also answers the question that the Monte Carlo subroutine only needs to be called two or three times to obtain converged steady state solutions. As a matter of fact, a case without radiation was considered and the differences in temperature, pressure and H₂O mass fraction between the two cases were found to be less than $\pm 1\%$.

The effects of radiation on the nozzle wall flux are quite different from the flowfield. It is noted the radiative wall flux is dominant over the conductive wall flux. Some specific results obtained for radiative and convective wall fluxes are presented here. It should be noted that the net radiative wall flux is the weighted average of the flux quantities in x and y direction in order

to reduce the errors introduced by the approximation of curved wall with ladder-like lines.

The effects of the equivalence ratio ϕ on q_{rw} and q_{cw} are illustrated in Fig. 5. For a specific ϕ value, q_{cw} is seen to increase first, reach to a peak and then go down. This is compatible with the trend in temperature variation as seen in Fig. 3(a). Unlike q_{cw} , q_{rw} is seen to increase with distance along the nozzle. This behavior is justifiable. In this study, the inlet and outlet of the flow are treated as the pseudoblack walls. The outlet flow temperatures are larger than the inlet flow temperatures and the outlet area is also bigger than the inlet area. In addition, as the flow goes downstream, the cross-sectional area of the flow increases. Consequently, the optical length increases. These two reasons result in higher value of q_{rw} as the distance from the inlet location increases. Comparing the values of q_{rw} and q_{cw} for each case, it is clear that the radiation is predominant. Even in the inlet region, q_{rw} is more than two times higher than q_{cw} . The results for three different equivalence ratios reveal different behavior for combustions with lean and rich mixtures. As ϕ increases from 0.6 to 1.0, the flow temperature and H₂O mass fraction increase by about 10% and 50% respectively, and pressure decreases by about 5%. The effects of these changes result in a sizable increase in the values of q_{rw} and q_{cw} . However, as ϕ increases from 1.0 to 1.4, the flow pressure decreases by about 5% and H₂O mass fraction increases by about 15%, but the temperature shows little change. This results in only a slight change in the values of q_{rw} and q_{cw} .

Figure 6 shows the effects of the nozzle wall temperature on q_{rw} and q_{cw} . The change of the nozzle wall temperature is found to have little influence on the combustion, and the flow temperature, pressure and H₂O mass fraction remain almost the same in most regions as T_w varies from 1500 K to 2100 K. As a result, the magnitude of the radiant energy absorbed on the wall is very close for the three cases with different nozzle wall temperatures. The value of q_{rw} is equal to the absorbed radiant energy minus the emitted radiant energy. So q_{rw} with higher wall temperature shows lower value as seen in Fig. 6. As for as q_{cw} is concerned, except in the entrance region, q_{cw} is seen to have a little change among the cases with different wall temperatures. This behavior is believed to be caused by the existence of turbulence.

The effects of the inlet flow temperature on q_{rw} and q_{cw} are demonstrated in Fig. 7. Inspection of the distribution of the q_{rw} value among the three cases reveals a very interesting feature of q_{rw} . The values of q_{rw} along the wall are not monotonically increased or decreased with T_i . The combined effects of temperature, pressure and H₂O mass fraction in the flow on radiation are responsible for this behavior. It is well known that increase of temperature, pressure and concentration of participating medium enhances radiation. As the T_i varies from 1500 K to 1800 K and then from 1800 K to 2100 K, the flow temperature increases by about 5% while the pressure and H₂O mass fraction decrease by about 10% and 15% respectively at each stage. An increase in temperature tries to reinforce the radiation while a decrease of pressure and H₂O mass fraction tries to reduce the radiation. So there exist two driving forces which compete with each other to affect the radiation. As a consequence of the competition, the lowest curve for q_{rw} is seen for the case with $T_i = 1800$ K and the highest values are observed for the case with $T_i = 1500$ K. Unlike q_{rw} , the values for q_{cw} are found to increase monotonically with T_i . This is because the convective wall flux is only dependent on temperature.

Finally, the effects of the nozzle size on q_{rw} and q_{cw} are illustrated in Fig. 8. By changing the nozzle length, the geometrically similar nozzles with different sizes can be obtained. As the nozzle length is reduced from 2.0 m to 1.0 m and then from 1.0 m to 0.5 m, the flow temperature and H₂O mass fraction are decreased by about 5% while the pressure is increased by about 2% at each stage. The effect of an increased pressure on the radiation is overshadowed by a decrease in the nozzle size, temperature and H₂O mass fraction. So, the lower values of q_{rw} are seen in the figure as the nozzle length is reduced. For the smaller nozzle size, the flow temperature may be lower, but the derivative of temperature is actually higher. Therefore, contrary to q_{rw} , the value q_{cw} is observed to increase with a decrease in the nozzle size. The opposite trend between the values of q_{rw} and q_{cw} brings a question about the role of radiation in heat transfer on the nozzle wall. With a decrease of nozzle size, the differences between the values of q_{rw} and q_{cw} are reduced and the dominance of radiation is diminished. In fact, at $L=0.5$, the value of q_{cw} is larger than the value of q_{rw} in some parts of the nozzle wall. It is expected that the radiation

will become less important and the conduction will replace the radiation as dominant mode of heat transfer on the nozzle wall if the nozzle size continues to reduce.

CONCLUSIONS

The radiative interactions have been investigated for chemically reacting supersonic flows of premixed hydrogen and air in an expanding nozzle. The MCM has been found to be very convenient and reliable tool to analyze radiative heat transfer in multi-dimensional nongray systems. For the chemically reacting supersonic flows, the effects of radiation on the flowfield can be neglected but the radiative effects on the heat transfer on the nozzle wall are significant. The extensive parametric studies on the radiative and conductive wall fluxes have demonstrated that the magnitude of the radiative and conductive wall fluxes are very sensitive to the equivalence ratio when the equivalence ratio is less than 1.0 but they may not be so when the equivalence ratio is higher than 1.0. The change in the wall temperature has little effect on the combustion. Thus, the radiative wall flux is decreased with an increase of wall temperature. But the conductive wall flux seems insensitive to the change of wall temperature. The radiative wall flux does not change monotonically with inlet flow temperature. Lower inlet flow temperature may yield higher radiative wall flux. The conductive wall flux, however, increases with an increase in the inlet flow temperature. The radiative wall flux decreases but the conductive wall flux increases with a reduction of nozzle size. For large size of nozzles, the radiative wall flux is dominant over the conductive wall flux. However, the situation may be reversed when the nozzle size is reduced.

ACKNOWLEDGMENTS

This work, in part, was supported by the NASA Langley Research Center through grant NAG-1-363 entitled "Institute for Computational and Applied Mechanics (ICAM)".

REFERENCES

1. Cess, R. D., Mighdoll, P., and Tiwari, S. N., 1967, "Infrared Radiative Heat Transfer in Nongray Gases," International Journal of Heat and Mass Transfer, Vol. 10, pp. 1521-1532.

2. Buckius, R. O., 1982, "The Effect of Molecular Gas Absorption on Radiative Heat Transfer with Scattering," Journal of Heat Transfer, Vol. 104, pp. 580–586.
3. Edwards, D. K., 1976, "Molecular Gas Band Radiation", Advances in Heat Transfer, Vol. 12, Academic Press, New York.
4. Soufiani, A., and Taine, J., 1987, "Application of Statistical Narrow-band Model to Coupled Radiation and Convection at High Temperature," International Journal of Heat and Mass Transfer, Vol. 30, No. 3, March 1987, pp. 437–447.
5. Zhang, L., Soufiani, A., and Taine, J., 1988, "Spectral Correlated and Non-correlated Radiative Transfer in a Finite Axisymmetric System Containing an Absorbing and Emitting Real Gas-particle Mixture," International Journal of Heat and Mass Transfer, Vol. 31, No. 11, November 1988, pp. 2261–2272.
6. Soufiani, A., Hartmann, J. M., and Taine, J., 1985, "Validity of Band-model Calculation for CO₂ and H₂O Applied to Radiative Properties and Conductive-radiative Transfer," Journal of Quantitative Spectroscopy and Radiative Transfer, Vol. 33, No. 3, March 1985, pp. 243–257.
7. Menart, J. A., Lee, H. S., and Kim, T. K., 1993, "Discrete Ordinates Solutions of Nongray Radiative Transfer with Diffusely Reflecting Walls," Journal of Heat Transfer, Vol. 115, February 1993, pp. 184–193.
8. Nelson, D. A., 1979, "Band Radiation within Diffuse-Walled Enclosures, Part I: Exact Solutions for Simple Enclosures," Journal of Heat Transfer, Vol. 101, February 1979, pp. 81–84.
9. Nelson, D. A., 1979, "Band Radiation within Diffuse-Walled Enclosures, Part II: An Approximate Method Applied to Simple Enclosures," Journal of Heat Transfer, Vol. 101, February 1979, pp. 85–89.
10. Liu, J., and Tiwari, S. N., 1994, "Investigation of Radiative Transfer in Nongray Gases Using a Narrow Band Model and Monte Carlo Simulation," Journal of Heat Transfer, Vol. 116, February 1994, pp. 160–166.

11. Soufiani, A., 1991, "Gas Radiation Spectral Correlated Approaches for Industrial Applications," in: Heat Transfer in Radiating and Combusting Systems, Carvalho, M. G., Lockwood, F., Taine, J., eds., Springer-Verlag, Berlin, 1991.
12. Mani, M. and Tiwari, S. N., 1988, "Investigation of Supersonic Chemically Reacting and Radiating Channel Flow," NASA CR-182726, January, 1988.
13. Tiwari, S. N., Chandrasekhar, R., Thomas, A. M. and Drummond, J. P., 1991, "Investigation of Chemically Reacting and Radiating Supersonic Internal Flows," AIAA-91-0572, January 1991.
14. Suehla, R. A. 1962, "Estimated Viscosities and Thermal Conductivities of Gases at High Temperatures," NASA TR R-132, 1962
15. Bird, R. B., Stewart, W. E. and Lightfoot, E. N., 1960, Transport Phenomena, John Wiley & Sons, New York, 1960.
16. McBride, B. J., Heimel, S., Ehlers, J. G. and Gordon, S., 1963, "Thermodynamic Properties to 6000 °K for 210 Substances Involving the First 18 Elements," NASA SP-3001, 1963.
17. Drummond, J. P., Rogers, R. C. and Hussaini, M. Y., 1986, "A Detailed Numerical Model of a Supersonic Reacting Mixing Layer," AIAA-86-1427, 1986.
18. Cai, J. C., Lee, H. S. and Patankar, S. V., 1993, "Treatment of Irregular Geometries Using a Cartesian-Coordinates-Based Discrete-Ordinates Method," Proceedings of the 29th National Heat Transfer Conference, Atlanta, Georgia, ASME HTD-Vol. 244, August 1993, pp. 49-54.
19. Malkmus, W., 1967, "Random Lorentz Band Model with Exponential-tailed S^{-1} Line-intensity Distribution Function," *Journal of the Optical Society of America*, Vol. 57, No. 3, pp. 323-329.
20. Ludwig, C. B., Malkmus, W., Reardon, J. E., and Thompson, J. A. L., 1973, "Handbook of Infrared Radiation from Combustion Gases," NASA SP-3080.

21. Hartmann, J. M., Levi Di Leon, R., and Taine, J., 1984, "Line-by-line and Narrow-band Statistical Model Calculations for H₂O," Journal of Quantitative Spectroscopy and Radiative Transfer, Vol. 32, No. 2, February 1984, pp. 119–127.
22. Godson, W. L., 1953, "The Evaluation of Infrared Radiation Fluxes Due to Atmospheric Water Vapor," Quarterly Journal of Royal Meteorological Society, Vol. 79, pp. 367–379.
23. Howell, J. R., 1968, "Application of Monte Carlo to Heat Transfer Problems," Advances in Heat Transfer, Vol. 5, Academic Press, New York.
24. Liu, J. and Tiwari, S. N., 1993, "Investigation of Two-dimensional Radiation Using a Narrow Band Model and Monte Carlo Method," Proceedings of the 29th National Heat Transfer Conference, Atlanta, Georgia, ASME HTD-Vol. 244, August 1993, pp. 21–31.
25. Drummond, J. P., Hussaini, M. Y. and Zang, T. A., 1986, "Spectral Methods for Modelling Supersonic Chemically Reacting Flowfields," AIAA Journal, Vol. 24, No. 9, September 1986, pp. 1461–1467.
26. Carpenter, M. H., 1988, "A Generalized Chemistry Version of SPARK," NASA CR-4196, 1988.
27. Siegel, R. and Howell, J. R., 1992, Thermal Radiation Heat Transfer, Hemisphere, New York, 3rd edition, 1992.

LIST OF TABLES AND FIGURES

Table 1	Hydrogen-air combustion mechanism (7 species, 7 reactions)
Fig. 1	Schematic diagram of nozzle
Fig. 2	Grid mesh for radiation simulation
Fig. 3(a)	Temperature contours in the nozzle
Fig. 3(b)	Pressure contours in the nozzle
Fig. 3(c)	H ₂ O mass fraction contours in the nozzle
Fig. 4	Radiative source distribution at three locations
Fig. 5	Comparison of radiative and conductive wall fluxes for three different equivalence ratios
Fig. 6	Comparison of radiative and conductive wall fluxes for three different wall temperatures
Fig. 7	Comparison of radiative and conductive wall fluxes for three different inlet temperatures
Fig. 8	Comparison of radiative and conductive wall fluxes for three different nozzle sizes

Table 1. Hydrogen-Air Combustion Mechanism (7 species, 7 reactions)

No.	Reaction	A	N	E
1	$\text{H}_2 + \text{O}_2 \rightarrow \text{OH} + \text{OH}$	1.70E+13	0.0	24233
2	$\text{H} + \text{O}_2 \rightarrow \text{OH} + \text{O}$	1.42E+14	0.0	8250
3	$\text{OH} + \text{H}_2 \rightarrow \text{H}_2\text{O} + \text{H}$	3.16E+07	1.8	1525
4	$\text{O} + \text{H}_2 \rightarrow \text{OH} + \text{H}$	2.07E+14	0.0	6920
5	$\text{OH} + \text{OH} \rightarrow \text{H}_2\text{O} + \text{O}$	5.50E+13	0.0	3523
6	$\text{H} + \text{OH} + \text{M} \rightarrow \text{H}_2\text{O} + \text{M}$	2.21E+22	-2.0	0
7	$\text{H} + \text{H} + \text{M} \rightarrow \text{H}_2 + \text{M}$	6.53E+17	-1.0	0

$$\frac{y_b}{L} = 0.25 \left[1.0 + \sin\left(\frac{\pi x}{2L}\right) \right]$$

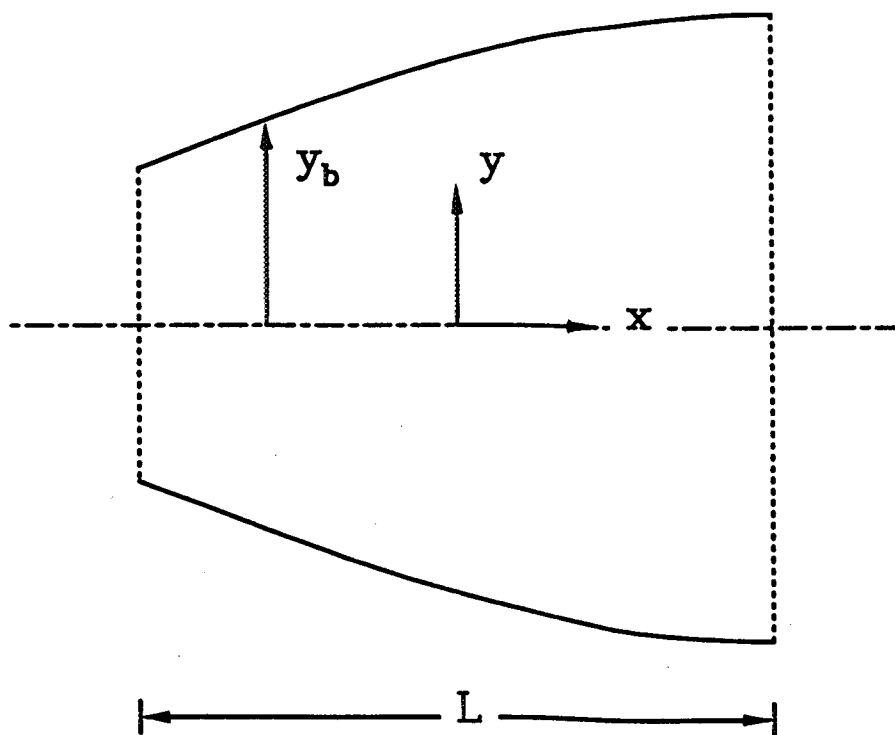


Fig.1 Schematic diagram of nozzle.

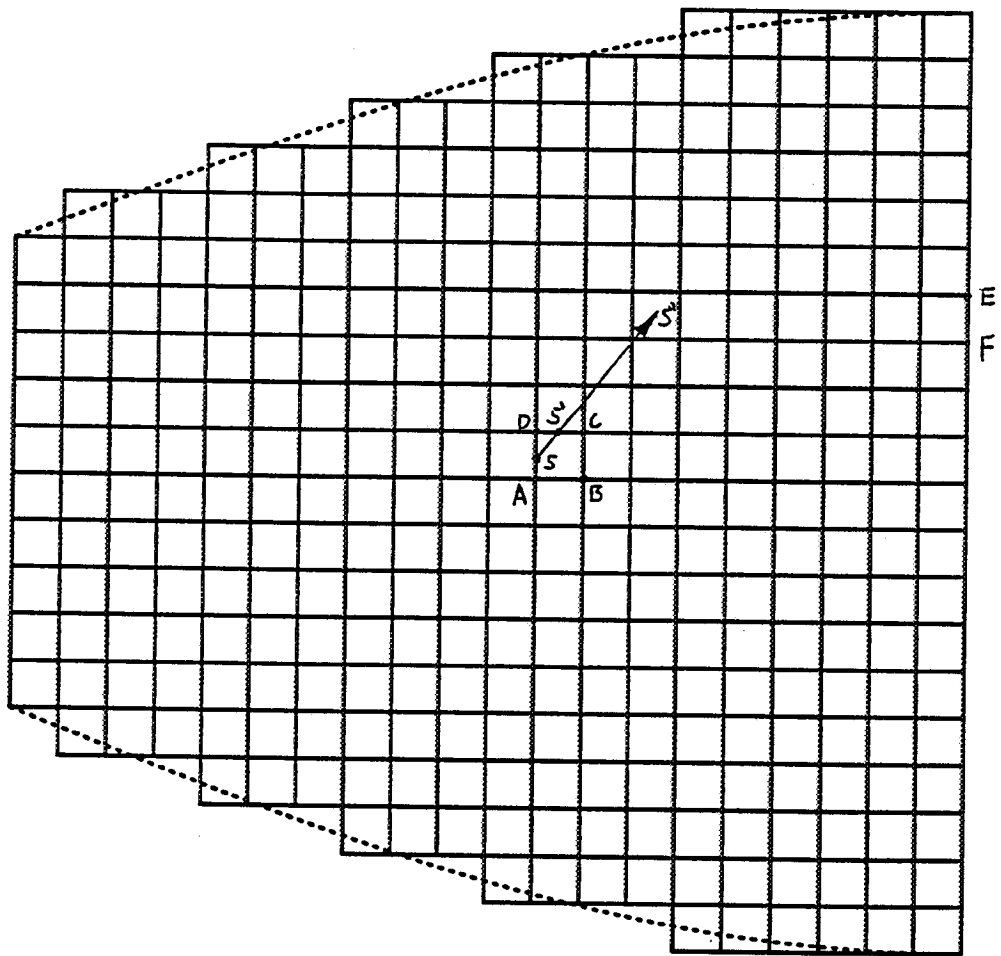


Fig.2. Grid mesh for radiation simulation (dashed lines are the actual walls).

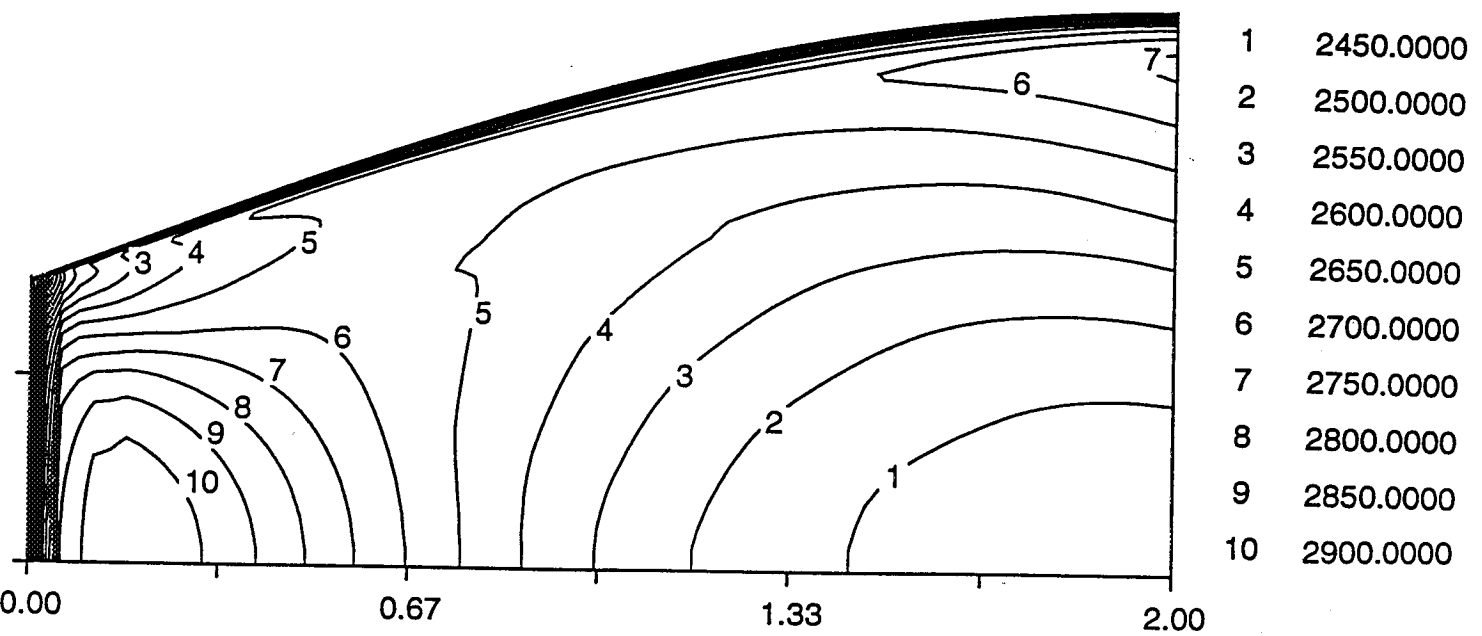


Fig.3(a) Temperature contours in the nozzle.

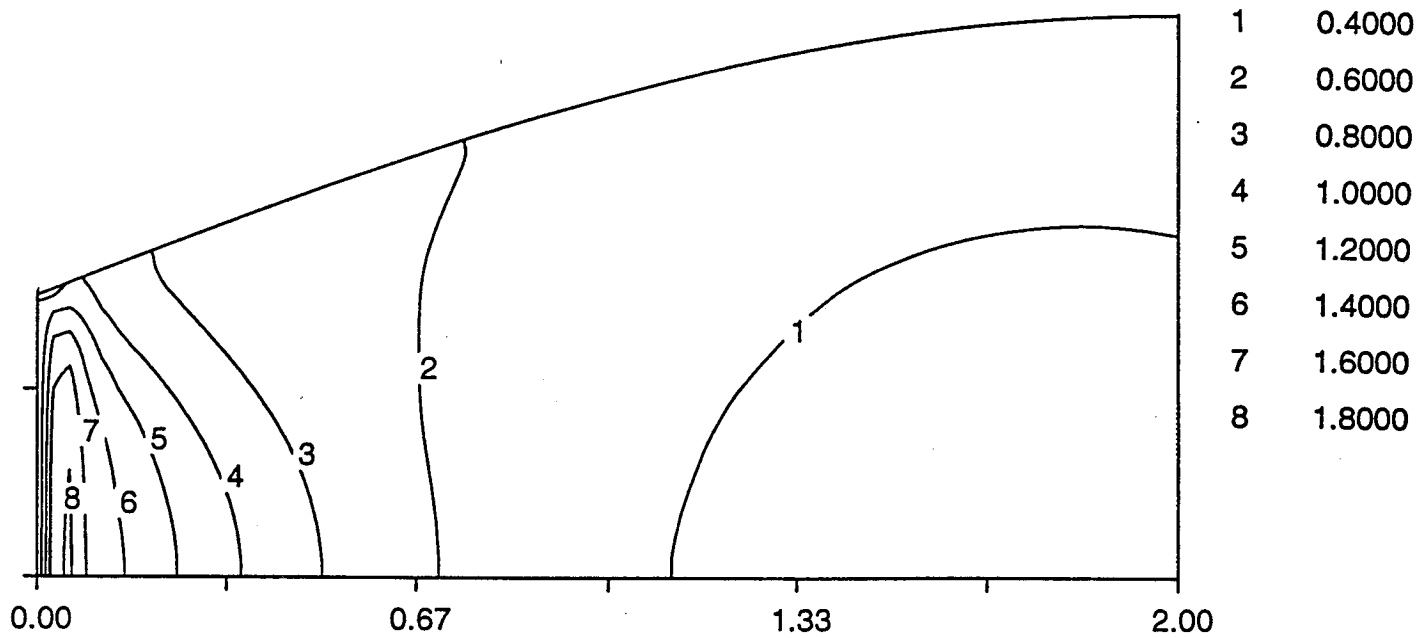


Fig.3(b) Pressure contours in the nozzle.

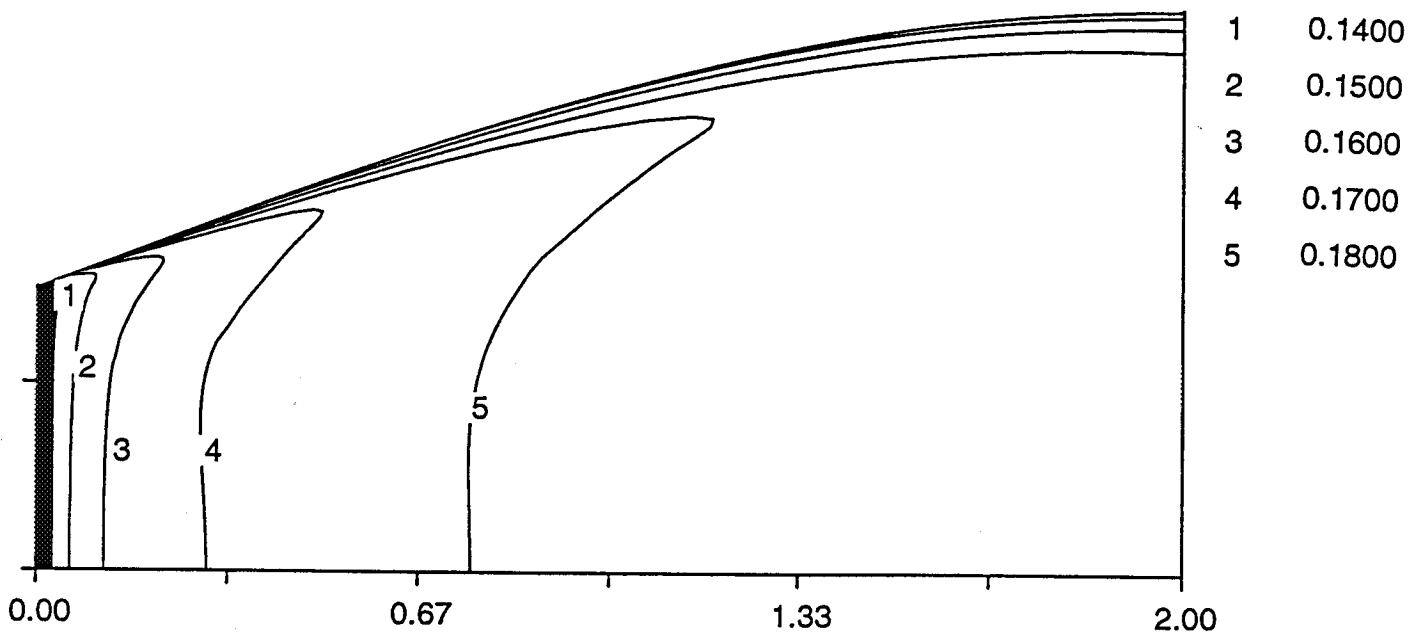


Fig.3(c) H₂O mass fraction contours in the nozzle.

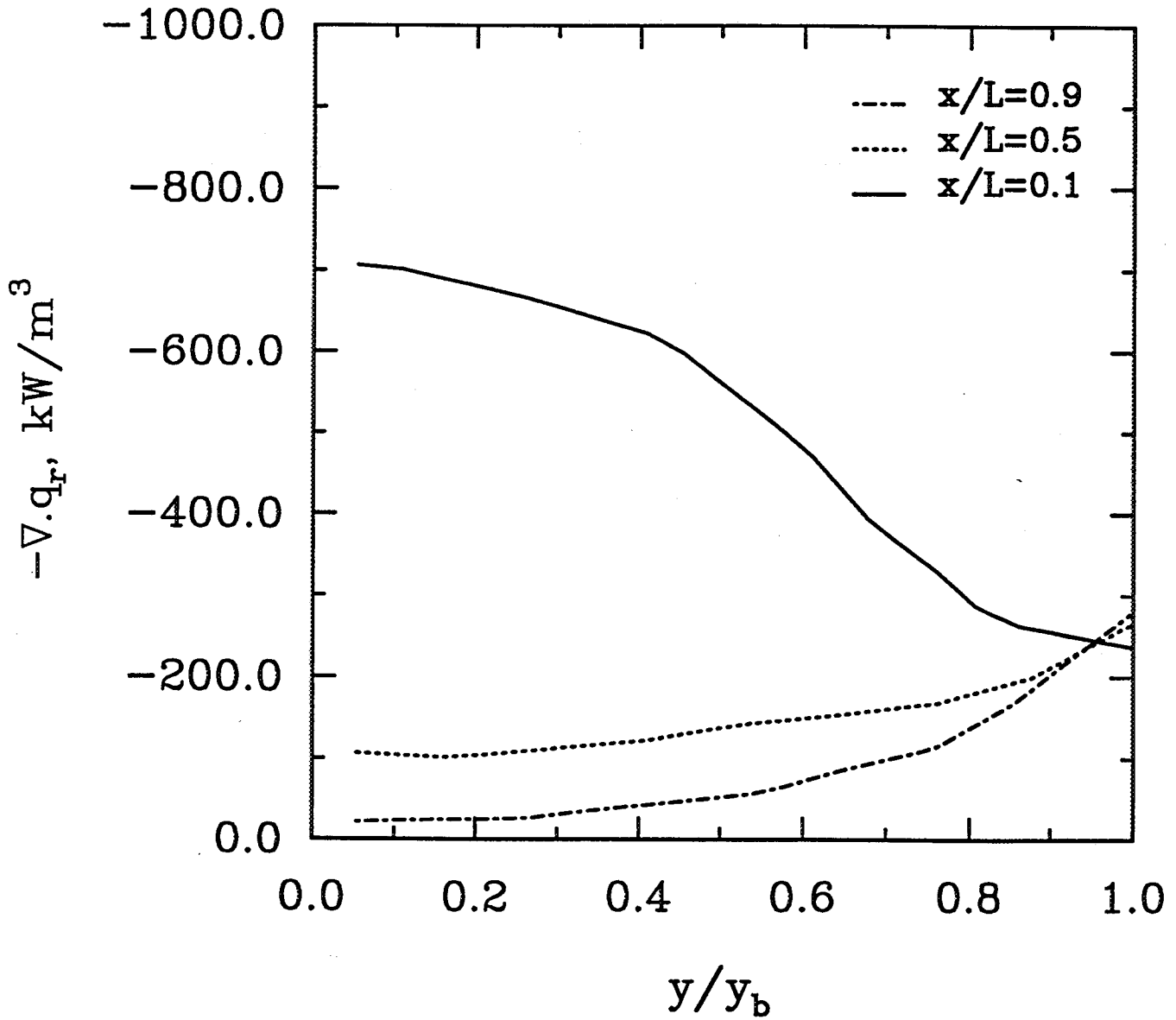


Fig.4 Radiative source distributions at three locations.

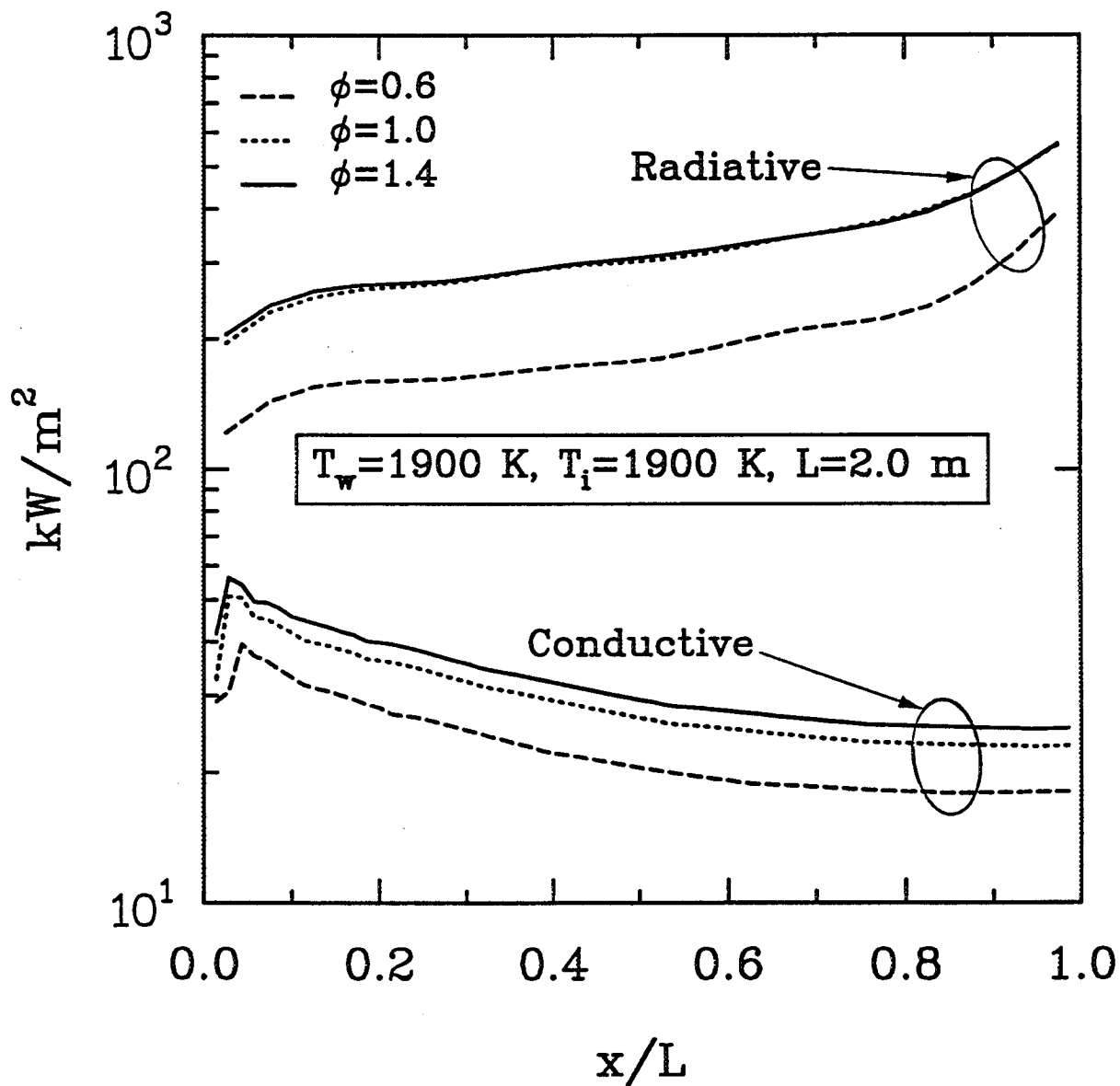


Fig.5 Comparison of radiative and conductive wall fluxes for three different equivalence ratios.

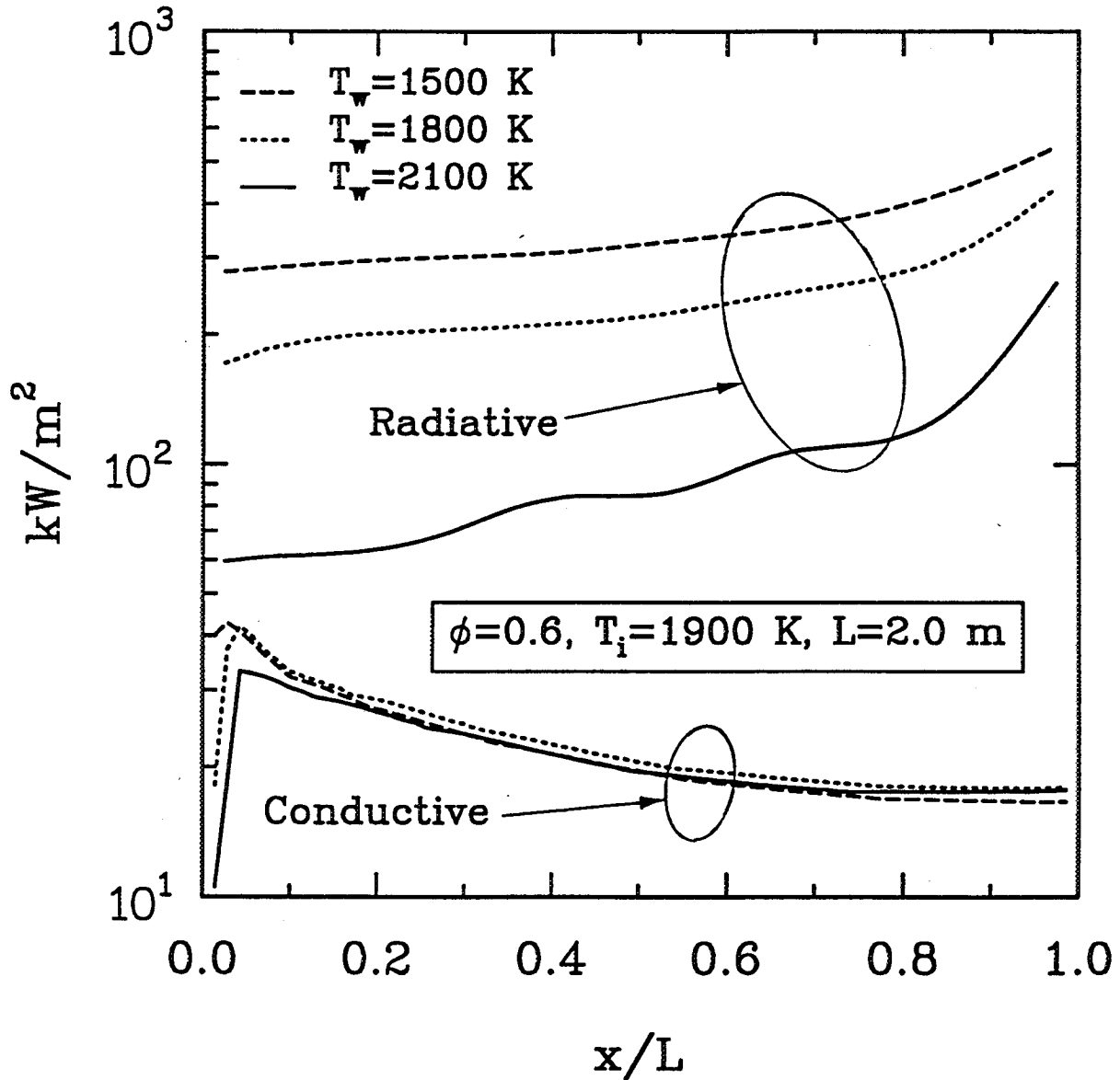


Fig.6 Comparison of radiative and conductive wall fluxes for three different wall temperatures.

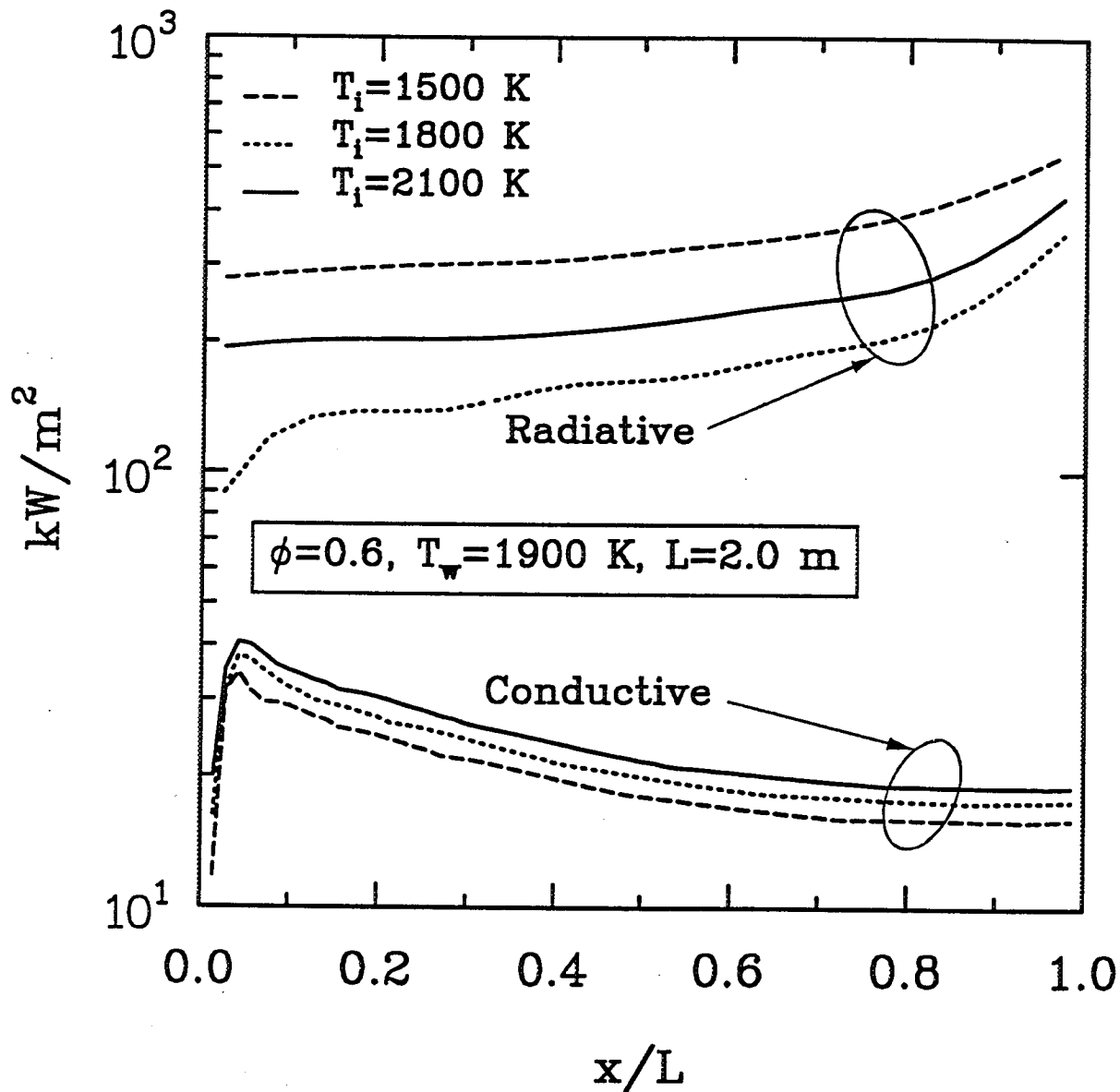


Fig.7 Comparison of radiative and conductive wall fluxes for three different inlet temperatures.

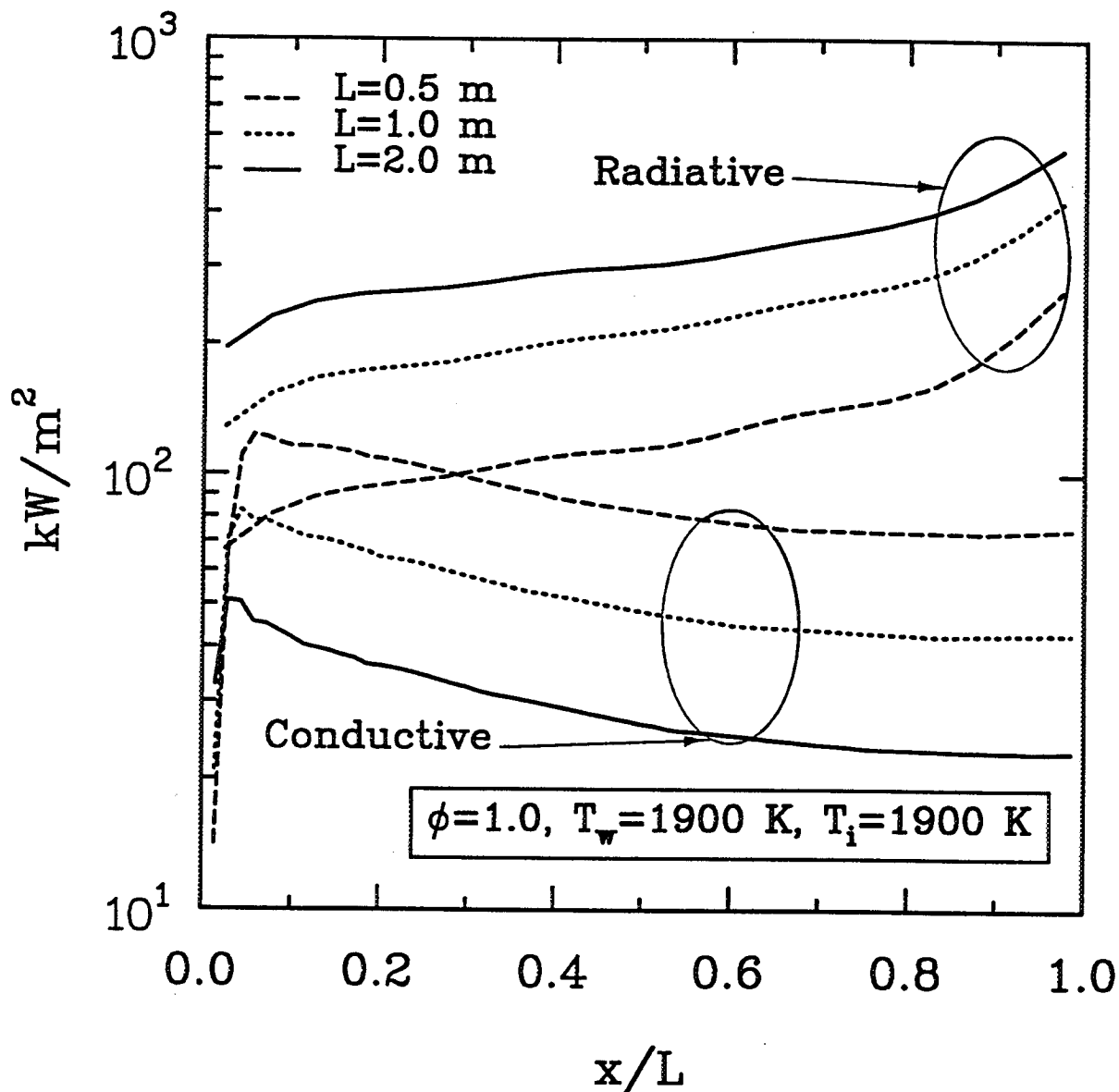
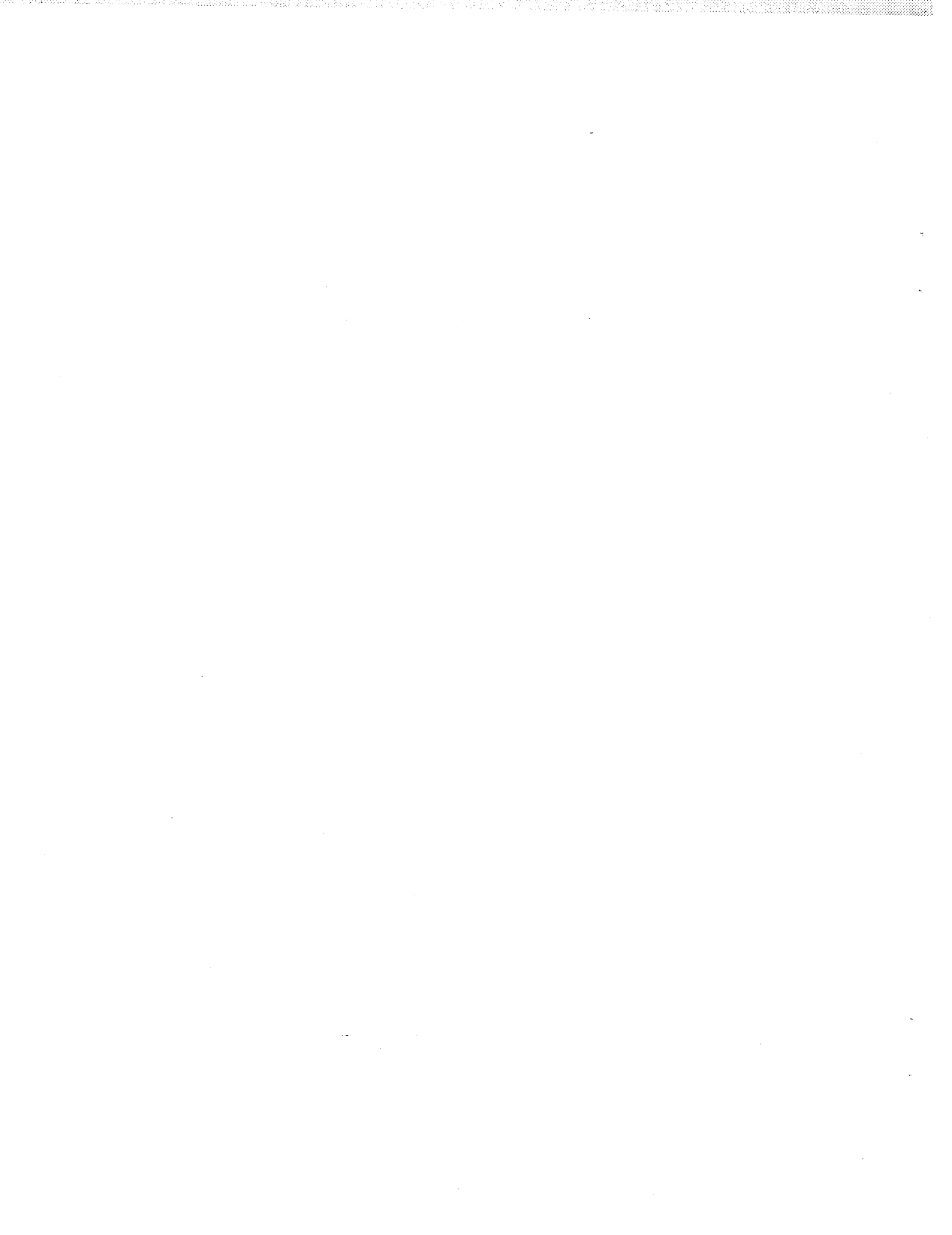


Fig.8 Comparison of radiative and conductive wall fluxes for three different nozzle sizes.





NOE

APPENDIX A

AIAA-94-2092

**RADIATIVE INTERACTIONS
IN CHEMICALLY REACTING
COMPRESSIBLE NOZZLE FLOWS
USING MONTE CARLO SIMULATIONS**

J. Liu and S. N. Tiwari

**Department of Mechanical Engineering
Old Dominion University
Norfolk, VA 23529-0247**

**6th AIAA/ASME Joint Thermophysics
and Heat Transfer Conference
June 20-23, 1994 / Colorado Springs, CO**



RADIATIVE INTERACTIONS IN CHEMICALLY REACTING COMPRESSIBLE NOZZLE FLOWS USING MONTE CARLO SIMULATIONS

J. Liu¹ and S. N. Tiwari²

Department of Mechanical Engineering
Old Dominion University, Norfolk, VA 23529-0247

ABSTRACT

The two-dimensional spatially elliptic Navier-Stokes equations have been used to investigate the radiative interactions in chemically reacting compressible flows of premixed hydrogen and air in an expanding nozzle. The radiative heat transfer term in the energy equation is simulated using the Monte Carlo method (MCM). The nongray model employed is based on the statistical narrow band model with an exponential-tailed inverse intensity distribution. The spectral correlation has been considered in the Monte Carlo formulations. Results obtained demonstrate that the radiative effects on the flow-field are minimal but radiative effects on the wall heat transfer are significant. Extensive parametric studies are conducted to investigate the effects of equivalence ratio, wall temperature, inlet flow temperature, and the nozzle size on the radiative and conductive wall fluxes.

NOMENCLATURE

Latin Symbols

A	reaction rate constant; also area, m ²
C	concentration, kg.mole/m ³
C _p	specific heat, J/(kg.K)
D	diffusion coefficient, m ² /s
E	total internal energy, J/kg; also activation energy, J/kg
f	mass fraction
g	Gibbs energy, J/(kg.K)
h	static enthalpy, J/kg
h ^R	base enthalpy, J/kg
L _ω	spectral radiative intensity, kW/(m ² .sr.cm ⁻¹)
k	thermal conductivity, J/(m.s.k); also line intensity to spacing ratio, cm ⁻¹ . atm ⁻¹
k _b	backward rate constant
k _{eq}	equilibrium constant
k _f	forward rate constant

L	nozzle length, m
m _ω	total number of narrow bands
M	molecular weight
N	temperature coefficient in reaction rate expression
N _s	number of species
N _r	number of reactions
P	gas pressure, atm
q _{cw}	conductive wall flux, kW/m ²
-∇·q _r	radiative source term, kW/m ³
q _{rw}	net radiative wall flux, kW/m ²
Q	radiative energy per unit volume, kW/m ³
R	gas constant, J/(kg.K); also random number
R _u	universal gas constant, J/(kg.K)
s, s', s''	position variables, m
t	time, s
T	absolute temperature, K
u	velocity in x direction, m/s
ū	diffusion velocity in x direction, m/s
v	velocity in y direction, m/s
v̄	diffusion velocity in y direction, m/s
v̄	diffusion velocity vector, m/s
ẇ	production rate of species, kg/(m ³ .s)
x	x-coordinate, m
X	mole fraction
y	y-coordinate, m
y _b	half height of cross sectional area of nozzle, m

Greek symbols

β	line width to spacing ratio
γ	stoichiometric coefficient; also half-width of an absorption line, cm ⁻¹
δ	equivalent line spacing, cm ⁻¹

¹ Graduate Research Assistant. Student Member AIAA.

² Eminent Professor. Associate Fellow AIAA.

θ	polar angle
μ	dynamic viscosity, kg/(m.s)
ξ, η	computational coordinates
ρ	density, kg/m ³
σ	normal stress, N/m ²
τ	shear stress, N/m ²
τ_{ω}	spectral transmittance
ϕ	equivalence ratio
ψ	azimuthal angle
ω	wavenumber, cm ⁻¹
Ω	solid angle

INTRODUCTION

There has been extensive research underway to develop hydrogen-fueled supersonic combustion ramjet (scramjet) propulsion systems for National Aero-Space Plane (NASP). A critical element in the design of scramjets is the detailed understanding of the complex flowfield present in different regions of the system over a range of operating conditions. Numerical modeling of the flow in various sections has shown to be a valuable tool for gaining insight into the nature of these flows.

In a hypersonic propulsion system, combustion takes place at supersonic speeds to reduce the deceleration energy loss. The products of hydrogen-air combustion are gases such as water vapor and hydroxyl radical. These species are highly radiatively absorbing and emitting. Thus, numerical simulation must be able to correctly handle the radiation phenomena associated with supersonic flows.

The study of radiative transmission in nonisothermal and inhomogeneous nongray gaseous systems requires a detailed knowledge of the absorption, emission and scattering characteristics of the specific species under investigation. In absorbing and emitting media, an accurate nongray model is of vital importance in the correct formulation of the radiative flux equations. The line-by-line models are theoretically the most precise models to treat radiative heat transfer. But solutions of the line-by-line formulation require considerably large computational resources. Currently, it is not practical to apply the line-by-line models in most engineering problems. The wide band models are the simplest nongray models and are extensively used in radiative heat transfer analyses [1, 2]. By far the most popular wide band model is the exponential wide band model developed by Edwards [3]. The exponential wide band model accounts for discrete absorption bands and spectral correlations resulting from the high resolution structure. However, the spectral discretization used in this model is too wide and it does

not take into account the low resolution correlations between intensities and transmissivities [4, 5]. Also, the case of partially reflecting walls cannot be correctly modelled with this approach [3]. Recently, the narrow band models have begun to receive a lot of attention due to the strong requirement for accurate simulation of radiation. Some narrow band models can compare favorably to the line-by-line calculations [4, 6], and they are much simpler than the line-by-line models. In addition, the narrow band models do not have disadvantages usually encountered with the wide band models.

Most of the existing analyses in radiative heat transfer start with the radiative transfer equation. Use of a narrow band model in this equation results in two types of spectral correlations [7]. One is the spectral correlation between the intensity and the transmittance within the medium. Another is the spectral correlation between the reflected component of the wall radiosity and the transmittance. In order to investigate the first type of spectral correlation, all the intermediate transmittances in each finite volume element of medium along the path the radiative energy travels must be calculated and stored to make a correlated calculation. In order to investigate the second type of spectral correlation, a series expansion of the wall radiosity is required [8, 9]. Essentially, this series expansion is utilized along with a technique for closure of the series. Consideration of the history of a finite number of reflections and approximating the remaining reflections by a closure method in the radiative transfer equation complicates the mathematical formulation and increases the computer time considerably. As the geometry considered becomes complicated, exact simulation of radiative heat transfer by most existing methods becomes very difficult for the cases with reflecting walls.

The MCM is not directly based on the radiative transfer equation to simulate radiative heat transfer. This results in the MCM having features different from the other methods for narrow band analysis. When the radiative energy is transmitted in the medium, the spectral correlation only occurs between the transmittances of two different segments of the same path in the statistical relationship for determining the absorption location of a energy bundle [10]. For the case with reflecting walls, Monte Carlo treatment with a narrow band model is similar to that with a gray model, and the second type of spectral correlation occurring in other methods does not exist. If the effect of scattering is included, a new type of spectral correlation occurs in the scattering term of the radiative transfer equation. Treatment of this spectral correlation will be far more complicated than the second type of spectral correlation mentioned earlier. In such cases, it has been indicated that only MCM can account for scattering in a correlated manner [11].

The objective of present study is to apply the Monte Carlo formulations with a narrow band model to investigate the effects of radiation on multi-dimensional chem-

ically reacting supersonic flows. Only a limited number of studies are available to investigate the interaction of radiation heat transfer in chemically reacting viscous and supersonic flows of molecular species. Mani and Tiwari [12] are the first to take into account the effects of radiation in chemically reacting supersonic flows. This work has been extended to include relatively more advanced chemistry models by Tiwari et al. [13]. In both of these studies, a tangent slab approximation was employed with a gray gas model. This approximation treats the gas layer as a one-dimensional slab in evaluation of the radiative flux. Obviously, it is impossible to obtain reliable quantitative predictions of radiation from this treatment. In this study, one of the most accurate nongray models available is employed and multi-dimensional radiative heat transfer is simulated using the MCM; the results of radiative flux are then incorporated in the Navier-Stokes equations. This procedure provides a more accurate prediction of the radiative effects than the previous studies.

GENERAL FORMULATION

Governing Equations

The physical model considered is a supersonic flow of premixed hydrogen and air in an expanding nozzle (Fig.1). The nozzle wall is defined, as noted, by a shifted sinusoidal curve. The inlet temperatures of hydrogen and air are considerably high so that the chemical reaction takes place in the entire flowfield. The products of hydrogen-air combustion include water vapor and hydroxyl radical. These species are highly absorbing and emitting. To simulate the flowfield accurately, all important phenomena such as chemistry, radiation and turbulence should be taken into account. In this study, the two-dimensional nozzle flow considered is described by the Navier Stokes and species continuity equations which take the form in the physical coordinates as

$$\frac{\partial U}{\partial t} + \frac{\partial F}{\partial x} + \frac{\partial G}{\partial y} = H \quad (1)$$

where vectors U, F, G and H are represented by

$$U = \begin{bmatrix} \rho \\ \rho u \\ \rho v \\ \rho E \\ \rho f_j \end{bmatrix} \quad (2)$$

$$F = \begin{bmatrix} \rho u \\ \rho u^2 - \sigma_x \\ \rho uv - \tau_{yx} \\ (\rho E - \sigma_x)u - \tau_{xy}v + q_x \\ \rho f_i(u + \tilde{u}_i) \end{bmatrix} \quad (3)$$

$$G = \begin{bmatrix} \rho v \\ \rho uv - \tau_{xy} \\ \rho v^2 - \sigma_y \\ (\rho E - \sigma_y)v - \tau_{yx}u + q_y \\ \rho f_i(v + \tilde{v}_i) \end{bmatrix} \quad (4)$$

$$H = \begin{bmatrix} 0 \\ 0 \\ 0 \\ -\nabla \cdot q_r \\ \dot{w}_i \end{bmatrix} \quad (5)$$

The other terms appearing in vectors F, G, and H are defined as

$$\sigma_x = -p + \lambda \left(\frac{\partial u}{\partial x} + \frac{\partial v}{\partial y} \right) + 2\mu \frac{\partial u}{\partial x} \quad (6)$$

$$\sigma_y = -p + \lambda \left(\frac{\partial u}{\partial x} + \frac{\partial v}{\partial y} \right) + 2\mu \frac{\partial v}{\partial y} \quad (7)$$

$$\tau_{xy} = \tau_{yx} = \mu \left(\frac{\partial u}{\partial x} + \frac{\partial v}{\partial y} \right) \quad (8)$$

$$q_x = -k \frac{\partial T}{\partial x} + \rho \sum_{i=1}^{N_s} h_i f_i \tilde{u}_i \quad (9)$$

$$q_y = -k \frac{\partial T}{\partial y} + \rho \sum_{i=1}^{N_s} h_i f_i \tilde{v}_i \quad (10)$$

$$E = -\frac{p}{\rho} + \frac{u^2 + v^2}{2} + \sum_{i=1}^{N_s} h_i f_i \quad (11)$$

$$h_i = h_i^R + \int_{T_R}^T C_{p,i} dT \quad (12)$$

$$p = \rho R_u T \sum_{i=1}^{N_s} \frac{f_i}{M_i} \quad (13)$$

where $\lambda = -\frac{2}{3}\mu$, $\mu = \mu_l + \mu_t$ and $k = k_l + k_t$. In this study the molecular viscosity μ_l and molecular thermal conductivity k_l are evaluated from the Sutherland's law [14]; the turbulent viscosity μ_t is evaluated from the Baldwin-Lomax model and the turbulent thermal conductivity k_t is calculated from the turbulent Prandtl number.

In Eqs. (1), only $(N_s - 1)$ species equations need to be considered since the mass fraction of the species is prescribed by satisfying the constraint equation

$$\sum_{i=1}^{N_s} f_i = 1 \quad (14)$$

The diffusion velocity of the i th species is obtained by solving the Stefan-Maxwell equation [15], neglecting the body force and thermal diffusion effects, as

$$\nabla X_i = \sum_{j=1}^{N_s} \left(\frac{X_i X_j}{D_{ij}} \right) (\tilde{V}_j - \tilde{V}_i) + (f_i - X_i) \left(\frac{\nabla p}{p} \right) \quad (15)$$

where $D_{ij} = D_{ij}^l + D_{ij}^t$. The molecular diffusion coefficient D_{ij}^l is obtained from the kinetic theory [15] and the turbulent diffusion coefficient D_{ij}^t is evaluated from the turbulent Schmidt number. Equation (15) has to be applied only to $(N_s - 1)$ species. The diffusion velocity for the remaining species is prescribed by satisfying the constraint equation $\sum_{i=1}^{N_s} f_i \tilde{V}_i = 0$, which ensures the consistency.

In the energy equation, it is noted that the radiative source term $-\nabla \cdot q_r$ has been moved to the right hand side and its treatment will be different from other terms. The simulation of this source term will be explained in detail later.

Thermodynamic and Chemistry Models

The specific heat of individual species $C_{p,i}$ is defined by a fourth-order polynomial in temperature,

$$\frac{C_{p,i}}{R} = A_i + B_i T + C_i T^2 + D_i T^3 + E_i T^4 \quad (16)$$

The values of the coefficients appearing in Eq. (16) are found in [16]. Knowing the specific heat of each species, the enthalpy of each species can be found from Eq. (12) and the total internal energy is computed from Eq. (11).

Chemical reaction rate expressions are usually determined by summing the contributions from each relevant reaction path to obtain the total rate of change of each species. Each path is governed by a law of mass action expression in which the rate constants can be determined from a temperature dependent Arrhenius expression. In vector H , the term $\dot{w}_i = M_i C_i$ represents the net rate of production of species i in all chemical reactions and is modelled as follows:

$$\sum_{i=1}^{N_s} \gamma_{ij} C_j \stackrel{k_{f_j}}{=} \sum_{i=1}^{N_s} \gamma_{ij}'' C_j; \quad j = 1, \dots, N_r \quad (17)$$

$$\begin{aligned} \dot{w}_i &= M_i C_i \\ &= M_i \sum_{j=1}^{N_r} (\gamma_{ij}'' - \gamma_{ij}') \\ &\times \left[k_{f_j} \prod_{m=1}^{N_s} C_m^{\gamma_{ij}'} - k_{b_j} \prod_{m=1}^{N_s} C_m^{\gamma_{ij}''} \right] \end{aligned} \quad (18)$$

Equation (17) represents an N_r step chemical reaction and Eq. (18) is the production rate for the i th species.

The reaction constants k_{f_j} and k_{b_j} are calculated from the following equations:

$$k_{f_j} = A_j T^{N_j} \exp\left(-\frac{E_j}{R_u T}\right); \quad j = 1, \dots, N_r \quad (19)$$

$$k_{b_j} = k_{f_j} / k_{eq,j}; \quad j = 1, \dots, N_r \quad (20)$$

The equilibrium constant appearing in Eq. (20) is given by

$$k_{eq,j} = \left(\frac{1}{R_u T} \right)^{\Delta n_j} \exp\left(\frac{-\Delta G_{R_j}}{R_u T}\right); \quad j = 1, \dots, N_r \quad (21)$$

where

$$\Delta n_j = \sum_{i=1}^{N_s} \gamma_{ij}'' - \sum_{i=1}^{N_s} \gamma_{ij}'; \quad j = 1, \dots, N_r \quad (22)$$

$$\Delta G_{R_j} = \sum_{i=1}^{N_s} \gamma_{ij}'' g_i - \sum_{i=1}^{N_s} \gamma_{ij}' g_i; \quad j = 1, \dots, N_r \quad (23)$$

$$\begin{aligned} \frac{g_i}{R_i} &= A_i (T - \ln T) - \frac{B_i}{2} T^2 - \frac{C_i}{6} T^3 - \frac{D_i}{12} T^4 \\ &- \frac{E_i}{20} T^5 + F_i - G_i T; \quad i = 1, \dots, N_r \end{aligned} \quad (24)$$

The forward rate for each reaction is determined from Eq. (19). The hydrogen-air combustion mechanism used in this work is from [17], but only seven species and seven reactions are selected for this study. The constants A_j , N_j and E_j for these reactions are listed in Table 1. The species Gibb's free energy expression Eq. (24) is obtained from the integrations of the specific heat $C_{p,i}$ and the coefficients in Eq. (24) are available in the same way as in Eq. (16).

RADIATION TRANSFER MODEL

The radiative effects on the nozzle flowfield arise through the term $-\nabla \cdot q_r$ in the energy equation and the radiative effects on the heat transfer on the nozzle walls arise through the term $q_{r,w}$. The expressions for both $-\nabla \cdot q_r$ and $q_{r,w}$ are very complicated integro-differential equations and they are usually treated separately from the governing equations. Before applying MCM to evaluate $-\nabla \cdot q_r$ and $q_{r,w}$, temperature, concentration of species, and pressure in the media should be assumed. Next, the participating media and the surrounding walls are divided into many quadrilateral volume elements and surface elements (Fig. 2(a)). Note that the inlet and outlet surfaces of the nozzle flow are treated as pseudoblack walls with the same temperature as the local gases.

For an arbitrarily chosen volume element with a volume δV and an arbitrarily chosen surface element

with an area δA in Fig. 2(a), the relations for $-\nabla \cdot q_r$ and $q_{r\omega}$ are expressed as

$$-\nabla \cdot q_r = \frac{Q_{V-\delta V} + Q_{A-\delta V} - Q_{\delta V}}{\delta V} \quad (25)$$

$$q_{r\omega} = \frac{Q_{V-\delta A} + Q_{A-\delta A} - Q_{\delta A}}{\delta A} \quad (26)$$

Here, $Q_{V-\delta V}$ and $Q_{V-\delta A}$ are the total radiant energy from the entire gas that are absorbed by the volume element δV and surface element δA , respectively; $Q_{A-\delta V}$ and $Q_{A-\delta A}$ are the total radiant energy from the bounding walls that are absorbed by δV and δA , respectively; $Q_{\delta V}$ and $Q_{\delta A}$ are the radiant energy emitted by δV and δA , respectively.

Evaluation of the terms $Q_{V-\delta V}$, $Q_{A-\delta V}$, $Q_{\delta V}$ and $Q_{V-\delta A}$ in Eqs. (25) and (26) requires a detailed knowledge of the absorption, emission and scattering characteristics of the specific gas. Several models are available in the literature to represent the absorption emission characteristics of molecular species. An accurate nongray model employed in this study is the statistical narrow band model with an exponential-tailed inverse intensity distribution. The transmittance predicted by this model in a homogeneous and isothermal column of length l due to gas species j , averaged over $[\omega - (\Delta\omega/2), \omega + (\Delta\omega/2)]$, is expressed as [19]

$$\bar{\tau}_\omega^j = \exp \left[-\frac{\bar{\beta}}{\pi} \left(\sqrt{1 + \frac{2\pi X_j p l \bar{k}}{\beta}} - 1 \right) \right] \quad (27)$$

where X_j represents the mole fraction of the absorbing species j ; \bar{k} and $\bar{\beta} = 2\pi\bar{\gamma}/\delta$ are the band model parameters which account for the spectral structure of the gas. The overbar symbol indicates that the quantity is averaged over a finite wavenumber interval $\Delta\omega$. Parameters \bar{k} and $1/\bar{\delta}$ generated from a line-by-line calculation have been published for H_2O , CO_2 , CO , OH , NO , and other species [6, 20, 21]. The mean half-width $\bar{\gamma}$ is obtained using the parameters suggested by Soufiani et al. [6]. The narrow band width considered is usually 25 cm^{-1} . Nonisothermal and inhomogeneous media are treated by using the Curtis-Godson approximation [22].

To simulate radiative heat transfer using the MCM, the total radiant energy in a volume element or surface element is assumed to be composed of many energy bundles. These energy bundles are similar to photons in their behavior. The histories of these energy bundles are traced from their point of emission to their point of absorption. What happens to each of these bundles depends on the emissive, scattering and absorptive behavior within the medium which is described by a set of statistical relationships. The detailed discussion of the MCM has been provided by Howell [23]. However, not all the statistical relationships given by Howell are applicable while using narrow band models. An important change

is the necessity to spectrally average radiative properties within each narrow band. This results in spectrally correlated formulations. For a volume element, the total emitted radiant energy and major statistical relationships in conjunction with a narrow band model are given by [24]

$$Q_{\delta V} = 4\pi \sum_{k=1}^{m_\omega} (\bar{\kappa}_{\omega^k} \bar{I}_{b\omega^k} \Delta\omega^k) dV \quad (28)$$

$$R_\omega = \frac{4\pi \sum_{k=1}^n (\bar{\kappa}_{\omega^k} \bar{I}_{b\omega^k} \Delta\omega^k) dV}{Q_{\delta V}}, \quad (\omega^{n-1} < \omega \leq \omega^n) \quad (29)$$

$$R_\theta = \frac{1 - \cos\theta}{2} \quad (30)$$

$$R_\psi = \frac{\psi}{2\pi} \quad (31)$$

$$R_l = \frac{L_m}{\ln \bar{\tau}_\omega(L_m)} \left(\frac{\partial \bar{\tau}_\omega}{\partial l} \right) \quad (32)$$

Here, $\bar{\kappa}_{\omega^k}$ is the mean absorption coefficient over the k th narrow band and is obtained as [25]

$$\bar{\kappa}_{\omega^k} \approx -\frac{\ln \bar{\tau}_{\omega^k}(L_m)}{L_m} \quad (33)$$

In the above equations, L_m is the mean beam length of the volume element; $I_{b\omega^k}$ is the Planck spectral blackbody intensity for the k th narrow band; θ and ψ are the polar and azimuthal angles of emission direction of an energy bundle, respectively; m_ω is the total number of narrow bands; R_ω , R_θ , R_ψ , R_l are random numbers which are uniformly distributed between zero and one. The statistical relationships for an energy bundle emitted from a surface element are similar to those given by Howell [23] and they are not listed here.

A large number of energy bundles is considered to satisfactorily represent the radiation emitted by a volume or surface element. The total number of energy bundles absorbed by each element multiplied by the energy per bundle gives the interchange of radiation among the volume and/or surface elements. The values of $-\nabla \cdot q_r$ and $q_{r\omega}$ can then be obtained from Eqs. (25) and (26), respectively. Substituting $-\nabla \cdot q_r$ into the energy equation, Eqs. (1) can be solved.

METHOD OF SOLUTION

Equations (1) is written in the the physical domain (x, y) and must be transformed to an appropriate computational domain (ξ, η) for solution. Using an algebraic grid generation technique, a highly clustered grid in the physical domain (near regions where high gradients exist) can be obtained as seen in Fig. 2(b). In the computational domain, Eqs. (1) are expressed as

$$\frac{\partial \hat{U}}{\partial t} + \frac{\partial \hat{F}}{\partial \xi} + \frac{\partial \hat{G}}{\partial \eta} = \hat{H} \quad (34)$$

where

$$\begin{aligned}\hat{U} &= UJ, & \hat{F} &= Fy_\eta - Gx_\eta \\ \hat{G} &= Gx_\xi - Fy_\xi, & \hat{H} &= HJ \\ J &= x_\xi y_\eta - y_\xi x_\eta\end{aligned}\quad (35)$$

Here J is the Jacobian of the transformation.

The governing equation system (34) can be stiff due to the kinetic source terms contained in the vector H . To deal with the stiff system, the kinetic source terms are computed implicitly in the temporally discrete form of Eq. (34). Once the temporal discretization is performed, the resulting system is spatially differenced using the explicit, unsplit MacCormack predictor-corrector schemes. This results in a spatially and temporally discrete, simultaneous system of equations at each grid point. Each simultaneous system is solved, subject to initial and boundary conditions. At the supersonic inflow boundary, all flow quantities are specified. At the supersonic outflow boundary, nonreflective boundary conditions are used. Only the upper half of the flow domain is computed, as the flow is assumed to be symmetric about the centerline of a two-dimensional nozzle. The upper boundary is treated as a solid wall. This implies a non-slip boundary condition. The wall temperature is given and wall species mass fractions and pressure are extrapolated from interior grid points, by assuming a non-catalytic wall as well as the boundary layer assumption on the pressure gradient. Symmetry boundary conditions are imposed at the lower boundary, that is, at the centerline. Initial conditions are obtained by specifying inlet flow conditions throughout the flowfield. The resulting set of equations is marched in time, until steady state solutions are achieved.

With consideration of radiative heat transfer, solution procedures employed in this study are summarized as following:

(a) First, the governing equations (1) is solved without consideration of radiation in terms of the modified MacCormack schemes;

(b) The steady solutions for temperature, pressure and species mass fractions are then used for Monte Carlo simulation. The computed radiative source term $-\nabla \cdot q_r$ from the MCM is based on a different grid from that used for Eqs. (1). Linear interpolation and extrapolation are employed for the transformation of $-\nabla \cdot q_r$ between the two grids;

(c) The transformed $-\nabla \cdot q_r$ is substituted into Eqs. (1), and Eqs. (1) is solved again. If the differences between two consecutive steady solutions are smaller than a designated tolerance, the computation ends. Otherwise, the steps (b) and (c) are repeated until solutions converge.

It is noted that there are two levels of numerical procedures employed here which result in two different iterative procedures. One is the numerical procedure for solving the Eqs. (1) and solutions iterate with time. The other is the numerical procedure for evaluating the

radiative source term using the MCM which results in the iteration of steady state solutions.

RESULTS AND DISCUSSION

Based on the theoretical and numerical analysis described earlier, a computer code has been developed to simulate two-dimensional supersonic chemically reacting and radiating nozzle flows on a Cray X-MP machine. The specific goal in this study is to investigate the effects of radiation on the flowfield and heat flux on the nozzle wall. By referring to [26], several problems have been considered. They contain four parameters: equivalence ratio of hydrogen and air, inlet flow temperature, wall temperature and nozzle size. Numerical solutions are obtained for a variety of combinations of these parameters. In each problem, flow is introduced to the nozzle at the same velocity of 1230 m/s and the same pressure of 1 atm. The grid size for solving the governing equations is 71×41 (upper half of the nozzle). Further refinement of the grid yields little changes in the results. For a given radiative source distribution, the residuals of Eqs. (1) are reduced by eight orders of magnitude in 3,000 iterations for a typical case and the steady state solutions are considered to have been obtained. The corresponding CPU time is about six minutes. To check the accuracy of computational scheme, a preliminary calculation has been carried out for chemically reacting nozzle flows without consideration of radiation. The results from this study show very good agreement with available solutions [26, 27].

For the temperature ranges considered, the important radiating species are OH and H_2O . But OH is a much less radiation participating species compared to H_2O . In addition, the concentration of OH is several times less than that of H_2O for the problems considered. So, the contribution of radiation from OH has been neglected in this study. For H_2O , there are five important absorption bands. All these bands have been taken into account and they consist of 295 narrow bands in the spectral range from 150 cm^{-1} to 7500 cm^{-1} [20]. In addition, for all the problems considered, the nozzle wall is assumed to be gray and the wall emissivity is taken to be 0.8.

To assure that the statistical results make sense in the Monte Carlo simulation, two requirements must be met. One is the accuracy of statistical results for a given grid. The other is the independence of the results on a grid. In this study, the designated statistical accuracy of the results is defined in such a way that when the relative statistical errors of results are less than $\pm 5\%$, the probability of the results lying within these limits is greater than 95%. Independence of the results on a grid is considered to have been achieved when the volume element number in the x direction is 20 and the volume element number in the y direction is 20 as shown in Fig. 2(a). For this grid, the total number of energy bundles had to be 5,000,000 and the required CPU time

was about one hours in order to meet the designated statistical accuracy in results for a typical problem. To test the independence of the Monte Carlo results on the grid, the same problem was investigated with a finer grid in which the volume element number in the x direction was increased to 30 and the volume element number in the y direction was doubled. To obtain the same accurate results, the total number of energy bundles had to increase to 15,000,000 and the corresponding CPU time increased to three hours. Comparing the solutions for the two different grids, it is found that the difference for the net radiative wall flux was never more than 2%, and the difference for the radiative source term was a little higher but less than 10%. In fact, the net radiative wall flux is the quantity we are most interested in, and its accuracy seems more important to us.

The grid considered for Monte Carlo computations in this study is coarser than that for numerical solutions of the energy equation. The intermediate values of the radiative source term within the grid for solutions of Eqs. (1) are obtained by interpolation and extrapolation. This should not introduce significant errors as the radiative source term is a slowly varying function compared to the temperature and its derivative [28]. The major CPU time consumed is in the Monte Carlo simulation. Fortunately, Monte Carlo subroutine only need to be called one to two times to obtain the converged steady state solutions. The reason for this will be explained later. It is believed that the computational time for Monte Carlo simulation could be reduced considerably if the code is vectorized and parallelized.

The radiative effects on the flowfield are investigated first. It is a common knowledge that the convective heat transfer is very strong for a supersonic flow. So the effects of radiation may not be very important. To determine these effects quantitatively, a typical problem is selected in which the equivalence ratio of hydrogen and air, wall temperature, inlet flow temperature and the nozzle length are taken to be $\phi=1.0$, $T_w=1900$ K, $T_i=1900$ K and $L=2.0$ m. The inlet species mass fractions are $f_{H_2} = 0.0283$, $f_{O_2} = 0.2264$, $f_{H_2O} = 0.0$, $f_{OH} = 0.0$, $f_O = 0.0$, $f_H = 0.0$, $f_{N_2} = 0.74529$. Figures 3(a)-3(c) show the temperature, pressure and H_2O mass fraction distributions. Knowing these information is essential to analyze the effect of radiative heat transfer. As the premixed mixture of hydrogen and air enters the nozzle, an exothermic chemical reaction takes place immediately, and the temperature and pressure increase abruptly and reach their peaks in a region closer to the inlet location (Figs. 3(a) and 3(b)). During this rapid change in temperature and pressure, the mass fraction of H_2O also experiences a big jump from zero to a value which varies little in the rest of the flow regime (Fig. 3(c)). As the flow continues to move downstream, supersonic expansion plays a major role, and the temperature and pressure are decreased. At the same time, the chemical reaction proceeds but it becomes very weak. This is why there is

a little change in H_2O mass fraction in the downstream region. Computation has been also conducted for other cases. Similar trends in results for temperature, pressure, and H_2O mass fractions for all species are also observed.

Figure 4 shows the radiative source distributions at three different locations for the case considered in Figs. 3(a)-3(b). At the location $x/L=0.1$, temperature and pressure are very high and there is more radiant energy emitted than absorbed. Consequently, the radiative source distribution is higher than at locations $x/L=0.5$ and 0.9 . The trend in results for $-\nabla \cdot q_r$ at the location $x/L=0.1$ is seen to be different from the results of other locations due to a decrease in temperature as the distance from the center line increases. The convective heat transfer distributions for the same locations as in Fig. 4 have been also calculated but they are not plotted in Fig. 4. This is because of large differences between the convective and radiative results; and also due to opposite signs for convective results at different locations. In most regions, the absolute value of the convective heat transfer is two or three orders of magnitude larger than the radiative source term. This situation does not change as long as the speed of the flow is very high. So, the effects of radiation on the flowfield are very weak for supersonic flows. This confirms our expectation and also answers the question that the Monte Carlo subroutine only needs to be called one or two times to obtain converged steady state solutions. As a matter of fact, a case without radiation was considered and the differences in temperature, pressure and H_2O mass fraction between the two cases were found to be less than $\pm 1\%$.

The radiative effects on the heat transfer on the nozzle walls are investigated next. Unlike the radiative effects on the flowfield, the effects of radiation on the nozzle wall flux are significant comparing those from conduction. Following results will demonstrate relative importance of radiative and conductive wall fluxes and how they change with equivalence ratio, wall temperature, inlet flow temperature, and nozzle size. Here, the conductive wall flux is defined as

$$q_{cw} = -k(T_w) \left(\frac{\partial T}{\partial n} \right)_{wall} \quad (36)$$

where n represents normal direction of the wall.

The effects of the equivalence ratio ϕ on q_{rw} and q_{cw} are illustrated in Fig. 5. For a specific ϕ value, q_{cw} is seen to increase first, reach to a peak and then go down. This is compatible with the trend in temperature variation as seen in Fig. 3(a). Unlike q_{cw} , q_{rw} is seen to increase with distance along the nozzle. This behavior is justifiable. In this study, the inlet and outlet of the flow are treated as the pseudoblack walls. The outlet flow temperatures are larger than the inlet flow temperatures and the outlet area is also bigger than the inlet area. In addition, as the flow goes downstream, the cross-sectional area of the flow increases. Consequently,

the optical length increases. These two reasons result in higher value of q_{rw} as the distance from the inlet location increases. Comparing the values of q_{rw} and q_{cw} for each case, it is clear that the radiation is predominant. Even in the inlet region, q_{rw} is more than two times higher than q_{cw} . The results for three different equivalence ratios reveal different behavior for combustions with lean and rich mixtures. As ϕ increases from 0.6 to 1.0, the flow temperature and H₂O mass fraction increase by about 10% and 50% respectively, and pressure decreases by about 5%. The effects of these changes result in a sizable increase in the values of q_{rw} and q_{cw} . However, as ϕ increases from 1.0 to 1.4, the flow pressure decreases by about 5% and H₂O mass fraction increases by about 15%, but the temperature shows little change. This results in only a slight change in the values of q_{rw} and q_{cw} .

Figure 6 shows the effects of the nozzle wall temperature on q_{rw} and q_{cw} . The change of the nozzle wall temperature is found to have little influence on the combustion, and the flow temperature, pressure and H₂O mass fraction remain almost the same in most regions as T_w varies from 1500 K to 2100 K. As a result, the magnitude of the radiant energy absorbed on the wall is very close for the three cases with different nozzle wall temperatures. The value of q_{rw} is equal to the absorbed radiant energy minus the emitted radiant energy. So q_{rw} with higher wall temperature shows lower value as seen in Fig. 6. As for as q_{cw} is concerned, except in the entrance region, q_{cw} is seen to have a little change among the cases with different wall temperatures. This behavior is believed to be caused by the existence of turbulence.

The effects of the inlet flow temperature on q_{rw} and q_{cw} are demonstrated in Fig. 7. Inspection of the distribution of the q_{rw} value among the three cases reveals a very interesting feature of q_{rw} . The values of q_{rw} along the wall are not monotonically increased or decreased with T_i . The combined effects of temperature, pressure and H₂O mass fraction in the flow on radiation are responsible for this behavior. It is well known that increase of temperature, pressure and concentration of participating medium enhances radiation. As the T_i varies from 1500 K to 1800 K and then from 1800 K to 2100 K, the flow temperature increases by about 5% while the pressure and H₂O mass fraction decrease by about 10% and 15% respectively at each stage. An increase in temperature tries to reinforce the radiation while a decrease of pressure and H₂O mass fraction tries to reduce the radiation. So there exist two driving forces which compete with each other to affect the radiation. As a consequence of the competition, the lowest curve for q_{rw} is seen for the case with $T_i=1800$ K and the highest values are observed for the case with $T_i=1500$ K. Unlike q_{rw} , the values for q_{cw} are found to increase monotonically with T_i . This is because the convective wall flux is only dependent on temperature.

Finally, the effects of the nozzle size on q_{rw} and

q_{cw} are illustrated in Fig. 8. By changing the nozzle length, the geometrically similar nozzles with different sizes can be obtained. As the nozzle length is reduced from 2.0 m to 1.0 m and then from 1.0 m to 0.5 m, the flow temperature and H₂O mass fraction are decreased by about 5% while the pressure is increased by about 2% at each stage. The effect of an increased pressure on the radiation is overshadowed by a decrease in the nozzle size, temperature and H₂O mass fraction. So, the lower values of q_{rw} are seen in the figure as the nozzle length is reduced. For the smaller nozzle size, the flow temperature may be lower, but the derivative of temperature is actually higher. Therefore, contrary to q_{rw} , the value q_{cw} is observed to increase with a decrease in the nozzle size. The opposite trend between the values of q_{rw} and q_{cw} brings a question about the role of radiation in heat transfer on the nozzle wall. With a decrease of nozzle size, the differences between the values of q_{rw} and q_{cw} are reduced and the dominance of radiation is diminished. In fact, at $L=0.5$, the value of q_{cw} is larger than the value of q_{rw} in some parts of the nozzle wall. It is expected that the radiation will become less important and the conduction will replace the radiation as dominant mode of heat transfer on the nozzle wall if the nozzle size continues to reduce.

CONCLUSIONS

The radiative interactions have been investigated for chemically reacting supersonic flows of premixed hydrogen and air in an expanding nozzle. The MCM has been found to be very convenient and reliable tool to analyze radiative heat transfer in multi-dimensional nongray systems. For the chemically reacting supersonic flows, the effects of radiation on the flowfield can be neglected but the radiative effects on the heat transfer on the nozzle wall are significant. The extensive parametric studies on the radiative and conductive wall fluxes have demonstrated that the magnitude of the radiative and conductive wall fluxes are very sensitive to the equivalence ratio when the equivalence ratio is less than 1.0 but they may not be so when the equivalence ratio is higher than 1.0. The change in the wall temperature has little effect on the combustion. Thus, the radiative wall flux is decreased with an increase of wall temperature. But the conductive wall flux seems insensitive to the change of wall temperature. The radiative wall flux does not change monotonically with inlet flow temperature. Lower inlet flow temperature may yield higher radiative wall flux. The conductive wall flux, however, increases with an increase in the inlet flow temperature. The radiative wall flux decreases but the conductive wall flux increases with a reduction of nozzle size. For large size of nozzles, the radiative wall flux is dominant over the conductive wall flux. However, the situation may be reversed when the nozzle size is reduced.

ACKNOWLEDGMENTS

This work, in part, was supported by the NASA Langley Research Center through grant NAG-1-363 entitled "Institute for Computational and Applied Mechanics (ICAM)".

REFERENCES

1. Cess, R. D., Mighdoll, P., and Tiwari, S. N., 1967, "Infrared Radiative Heat Transfer in Nongray Gases," International Journal of Heat and Mass Transfer, Vol. 10, pp. 1521-1532.
2. Buckius, R. O., 1982, "The Effect of Molecular Gas Absorption on Radiative Heat Transfer with Scattering," Journal of Heat Transfer, Vol. 104, pp. 580-586.
3. Edwards, D. K., 1976, "Molecular Gas Band Radiation", Advances in Heat Transfer, Vol. 12, Academic Press, New York.
4. Soufiani, A., and Taine, J., 1987, "Application of Statistical Narrow-band Model to Coupled Radiation and Convection at High Temperature," International Journal of Heat and Mass Transfer, Vol. 30, No. 3, March 1987, pp. 437-447.
5. Zhang, L., Soufiani, A., and Taine, J., 1988, "Spectral Correlated and Non-correlated Radiative Transfer in a Finite Axisymmetric System Containing an Absorbing and Emitting Real Gas-particle Mixture," International Journal of Heat and Mass Transfer, Vol. 31, No. 11, November 1988, pp. 2261-2272.
6. Soufiani, A., Hartmann, J. M., and Taine, J., 1985, "Validity of Band-model Calculation for CO₂ and H₂O Applied to Radiative Properties and Conductive-radiative Transfer," Journal of Quantitative Spectroscopy and Radiative Transfer, Vol. 33, No. 3, March 1985, pp. 243-257.
7. Menart, J. A., Lee, H. S., and Kim, T. K., 1993, "Discrete Ordinates Solutions of Nongray Radiative Transfer with Diffusely Reflecting Walls," Journal of Heat Transfer, Vol. 115, February 1993, pp. 184-193.
8. Nelson, D. A., 1979, "Band Radiation within Diffuse-Walled Enclosures, Part I: Exact Solutions for Simple Enclosures," Journal of Heat Transfer, Vol. 101, February 1979, pp. 81-84.
9. Nelson, D. A., 1979, "Band Radiation within Diffuse-Walled Enclosures, Part II: An Approximate Method Applied to Simple Enclosures," Journal of Heat Transfer, Vol. 101, February 1979, pp. 85-89.
10. Liu, J., and Tiwari, S. N., 1994, "Investigation of Radiative Transfer in Nongray Gases Using a Narrow Band Model and Monte Carlo Simulation," Journal of Heat Transfer, Vol. 116, February 1994, pp. 160-166.
11. Soufiani, A., 1991, "Gas Radiation Spectral Correlated Approaches for Industrial Applications," in: Heat Transfer in Radiating and Combusting Systems, Carvalho, M. G., Lockwood, F., Taine, J., eds., Springer-Verlag, Berlin, 1991.
12. Mani, M. and Tiwari, S. N., 1988, "Investigation of Supersonic Chemically Reacting and Radiating Channel Flow," NASA CR-182726, January, 1988.
13. Tiwari, S. N., Chandrasekhar, R., Thomas, A. M. and Drummond, J. P., 1991, "Investigation of Chemically Reacting and Radiating Supersonic Internal Flows," AIAA-91-0572, January 1991.
14. Suehla, R. A. 1962, "Estimated Viscosities and Thermal Conductivities of Gases at High Temperatures," NASA TR R-132, 1962
15. Bird, R. B., Stewart, W. E. and Lightfoot, E. N., 1960, Transport Phenomena, John Wiley & Sons, New York, 1960.
16. McBride, B. J., Heibel, S., Ehlers, J. G. and Gordon, S., 1963, "Thermodynamic Properties to 6000 °K for 210 Substances Involving the First 18 Elements," NASA SP-3001, 1963.
17. Drummond, J. P., Rogers, R. C. and Hussaini, M. Y., 1986, "A Detailed Numerical Model of a Supersonic Reacting Mixing Layer," AIAA-86-1427, 1986.
18. Cai, J. C., Lee, H. S. and Patankar, S. V., 1993, "Treatment of Irregular Geometries Using a Cartesian-Coordinates-Based Discrete-Ordinates Method," Proceedings of the 29th National Heat Transfer Conference, Atlanta, Georgia, ASME HTD-Vol. 244, August 1993, pp. 49-54.
19. Malkmus, W., 1967, "Random Lorentz Band Model with Exponential-tailed S⁻¹ Line-intensity Distribution Function," Journal of the Optical Society of America, Vol. 57, No. 3, pp. 323-329.
20. Ludwig, C. B., Malkmus, W., Reardon, J. E., and Thompson, J. A. L., 1973, "Handbook of Infrared Radiation from Combustion Gases," NASA SP-3080.
21. Hartmann, J. M., Levi Di Leon, R., and Taine, J., 1984, "Line-by-line and Narrow-band Statistical Model Calculations for H₂O," Journal of Quantitative Spectroscopy and Radiative Transfer, Vol. 32, No. 2, February 1984, pp. 119-127.
22. Godson, W. L., 1953, "The Evaluation of Infrared Radiation Fluxes Due to Atmospheric Water Vapor," Quarterly Journal of Royal Meteorological Society, Vol. 79, pp. 367-379.
23. Howell, J. R., 1968, "Application of Monte Carlo to Heat Transfer Problems," Advances in Heat Transfer, Vol. 5, Academic Press, New York.
24. Liu, J. and Tiwari, S. N., 1994, "Spectrally Correlated Monte Carlo Formulations for Radiative Transfer in Multi-dimensional Systems," Submitted for publica-

tion in Journal of Thermophysics and Heat Transfer.

25. Kim, T. K., Menart, J. A., and Lee, H. S., 1991, "Nongray Radiative Gas Analyses Using the S-N Discrete Ordinates Method," Journal of Heat Transfer, Vol. 113, November 1991, pp. 946-952.

26. Drummond, J. P., Hussaini, M. Y. and Zang, T. A., 1986, "Spectral Methods for Modelling Supersonic

Chemically Reacting Flowfields," AIAA Journal, Vol. 24, No. 9, September 1986, pp. 1461-1467.

27. Carpenter, M. H., 1988, "A Generalized Chemistry Version of SPARK," NASA CR-4196, 1988.

28. Siegel, R. and Howell, J. R., 1992, Thermal Radiation Heat Transfer, Hemisphere, New York, 3rd edition, 1992.

Table 1 Hydrogen-air combustion mechanism (7 species, 7 reactions)

No.	Reaction	A	N	E
1	$H_2 + O_2 \rightarrow OH + OH$	1.70E+13	0.0	24233
2	$H + O_2 \rightarrow OH + O$	1.42E+14	0.0	8250
3	$OH + H_2 \rightarrow H_2O + H$	3.16E+07	1.8	1525
4	$O + H_2 \rightarrow OH + H$	2.07E+14	0.0	6920
5	$OH + OH \rightarrow H_2O + O$	5.50E+13	0.0	3523
6	$H + OH + M \rightarrow H_2O + M$	2.21E+22	-2.0	0
7	$H + H + M \rightarrow H_2 + M$	6.53E+17	-1.0	0

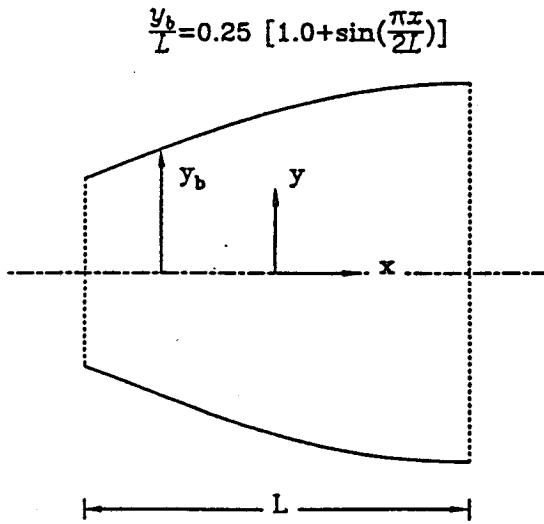


Fig.1 Schematic diagram of nozzle.

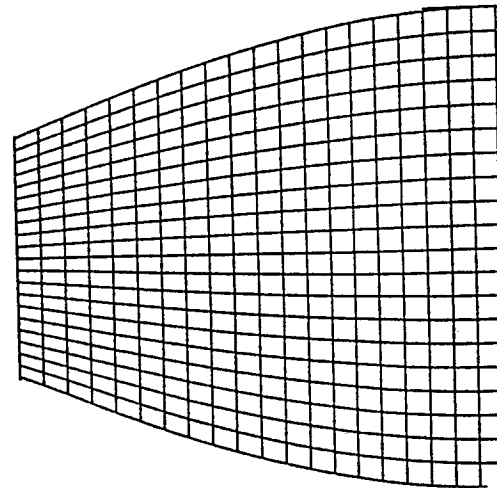


Fig.2(a) Grid mesh for radiation simulation.

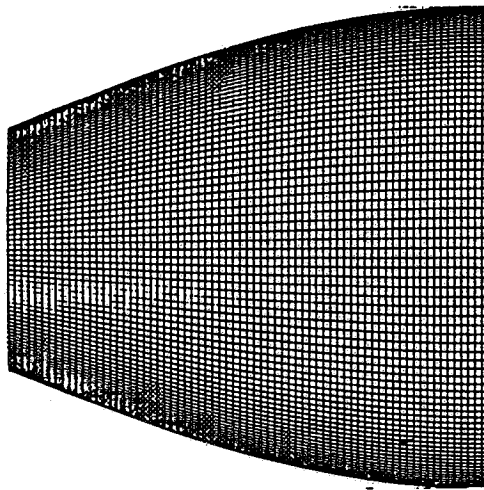


Fig.2(b) Grid mesh for flowfield simulation.

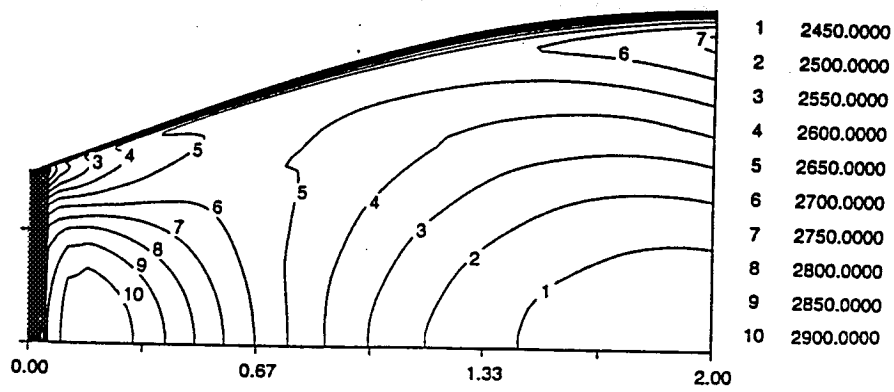


Fig.3(a) Temperature contours in the nozzle.

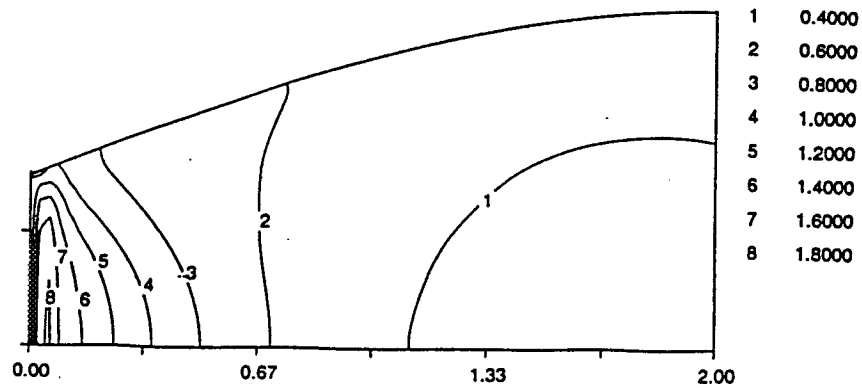


Fig.3(b) Pressure contours in the nozzle.

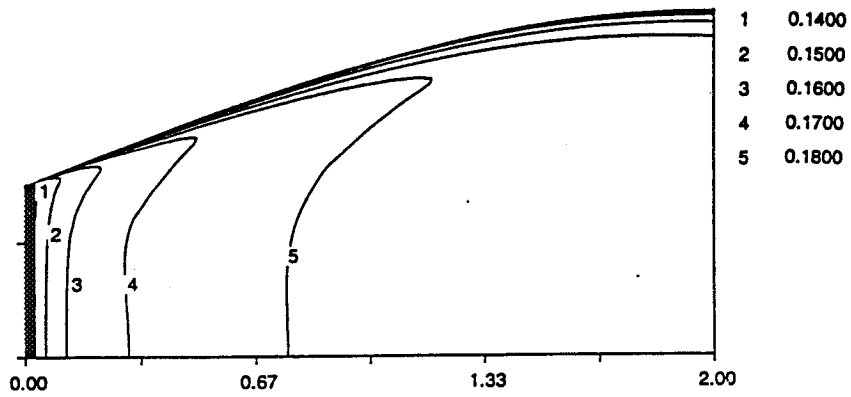


Fig.3(c) H₂O mass fraction contours in the nozzle.

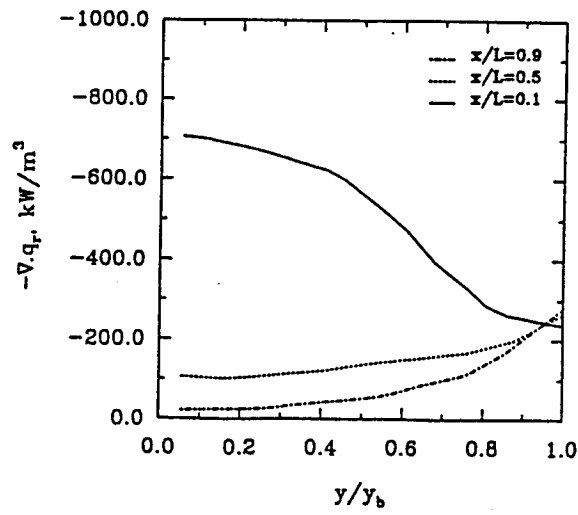


Fig.4 Radiative source distributions at three locations.

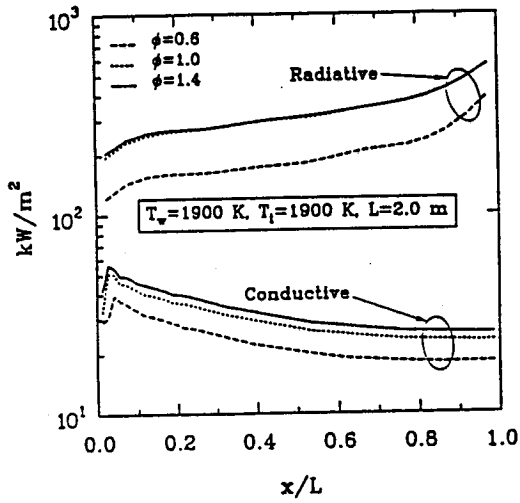


Fig.5 Comparison of radiative and conductive wall fluxes for three different equivalence ratios.

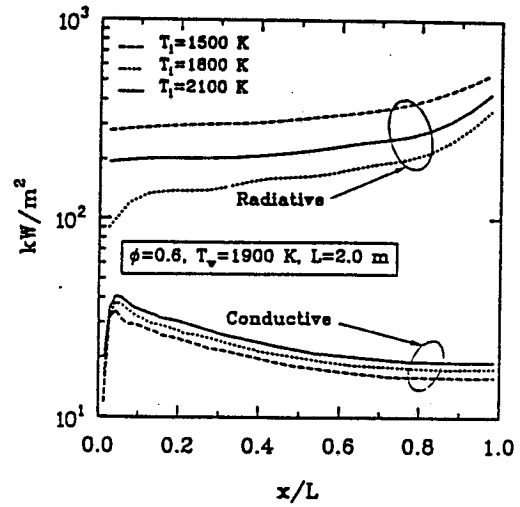


Fig.7 Comparison of radiative and conductive wall fluxes for three different inlet temperatures.

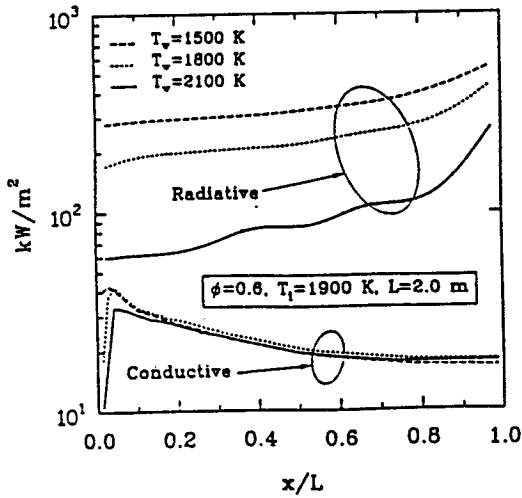


Fig.6 Comparison of radiative and conductive wall fluxes for three different wall temperatures.

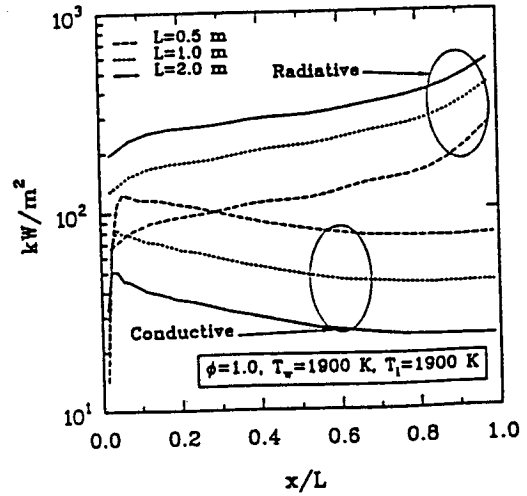


Fig.8 Comparison of radiative and conductive wall fluxes for three different nozzle sizes.